Multifractal and multiscale entropy scaling of in-situ soil moisture time series: Study of SMOSMANIA network data, southwestern France

Sébastien Verrier

Multifractal and Multiscale Entropy scaling of in-situ soil moisture time series: study of SMOSMANIA network data, southwestern France

Sébastien Verrier*

*Affiliation : (1) CESBIO, Université de Toulouse, CNES, CNRS, INRA, IRD, UPS, Toulouse, France.

(2) IUT Paul Sabatier, Auch, France

Correspondance : Dr. Sébastien Verrier, sebastien.verrier@iut-tlse3.fr

1 Introduction

Soil moisture is a key variable in hydrology, meteorology and biosphere science. It is the result of a strongly heterogeneous atmospheric forcing, i.e. rainfall, and of the interaction of other processes like evaporation, transpiration, or infiltration. Consequently, soil moisture is subject to strong and possibly quick variations and is heterogeneous in space and time. This results in potential difficulties in sampling strategies since sensors have their own limitations in terms of observable scales (Vereecken et al., 2014). For instance, operating passive L-band radiometers like those of SMOS (Kerr et al., 2010; 2016) and SMAP (Entekhabi et al., 2010) missions can provide continental daily coverage of soil moisture variability but their spatial resolution is limited to pixels of about 50x50 km². Airborne missions can provide more details about spatial variability but data are available over limited areas and a very limited amount of time (i.e. when the mission is operated). Conversely, in-situ sensors have the ability to give a very local estimate of soil moisture over small (hourly or sub-hourly) time steps but their observations are difficult to upscale or to extrapolate to other locations. This resolution mismatch may be somewhat reduced by applying downscaling methods to satellite data (e.g., Merlin et al., 2008; 2011), but the problem is still not fully solved since downscaled products have still coarse (kilometric) resolutions in comparison to the small spatial domain seen by an in-situ sensor.

An alternative approach is to try to characterize the spatial and temporal variability of soil moisture with intrinsically multiscale statistical formalisms. The idea behind such formalisms relies on the fact that a complex, heterogeneous signal or random process may hide remarkable symmetries. In this context, we may look for statistical estimators that could be related to the process resolution by simple analytical laws. Such scaling properties are accurately followed by various geophysical variables (Lovejoy, Schertzer et al., 2008; Lovejoy and Schertzer, 2006, 2010; Gagnon et al., 2006; Tessier et al., 1993). In many cases, these properties are even related to the concepts of scale invariance and fractality (some of these concepts will be defined in Section 2).

In geophysics, the characterization of scaling laws may be useful for several kinds of applications such as: (i) comparing the variability of measurements collected by sensors operating at different resolutions, (ii) evaluating a numerical model (such as a General Circulation Model or a Land Surface Model) that should be able to reproduce some scaling features of the observations (e.g., Lovejoy et al., 2013; Verrier et al., 2014), (iii) constraining statistical downscaling methods (Gires et al., 2012) to respect the observed scaling laws.

In the context of soil moisture, existing studies already evidenced the existence of fractal-like scaling in space and in time. In particular, remote sensing data have been used by several authors in order to investigate fractal properties across space scales. Kim and Barros (2002a, 2002b) analyzed airborne soil moisture estimates from the Southern Great Plains 1997 experiment and proposed a monofractal approach for downscaling soil moisture from 10 km to 1km resolution. Multifractal variants of the latter approach have been proposed later by Mascaro et al. (Mascaro and Vivoni, 2010, 2012; Mascaro et al., 2010, 2011) based on (partly similar) airborne remote sensing data sets. Several analyses have also been performed on satellite images. For instance, Lovejoy, Tarquis et al. (2008) have shown that both MODIS radiances and surface soil moisture index exhibit scaling and multifractal properties (based on a case study over central Spain).

In the time domain, Katul et al. (2007) also identified the existence of spectral scaling properties based on relatively long-term in-situ acquisitions (8 years of hourly data) at one specific station. The authors also proposed a physical approach to justify the existence of these properties, especially taking into account the integrative nature of soil water content with respect to its meteorological forcing.

In the following, scaling analysis tools are applied to surface soil moisture time series collected by a network of probes, SMOSMANIA. Overall, the SMOSMANIA network consists of about 20 stations located in South-Western and South-Eastern France. Capacitive measurements of hourly soil moisture have been done continuously during several years at stations belonging to the Météo-

France operational observation network. This makes these measurements suitable for scaling analyses due to the wide range of time scales covered by the data. Moreover, the network design is based on a compromise between a large spatial coverage and a moderate distance between probes. Finally, all probes are located at places with relatively normalized conditions (flat areas, fallow vegetation, low or moderate altitude) since they are co-located with operational meteorological stations operated by Météo-France (Calvet et al., 2007; Albergel et al., 2010).

In this paper, a scaling analysis of eight-year long SMOSMANIA time series is proposed, based on spectral and multifractal analysis tools. The objective will be to try to identify whether scaling properties are present and over which scale range. Scaling will also be investigated in terms of complexity analysis by computing the multiscale entropy (MSE) of the different time series.

The rest of the paper is structured as follows. In Section 2, theoretical notions related to spectral scaling, multifractal scaling, and MSE are recalled. Then the dataset is presented in Section 3. Spectral analysis results are then presented in Section 4, followed by the multifractal analysis of the dataset in Section 5. MSE analysis of the data is detailed in Section 6. Then, in the subsequent Section 7, the expected relationship between MSE and multifractal scaling parameters is investigated with the help of numerical simulations and discussed. Finally, I conclude in Section 8.

2 Theoretical background

2.1 Spectral scaling

Scale invariance consists of a family of generic properties exhibited by many geophysical datasets (time series, 2D/3D fields). The concept is closely related to the concept of fractality that has been investigated and popularized by B. Mandelbrot (e.g., Mandelbrot, 1983). In the context of stochastic modeling of geophysical processes, scaling may be typically detected by investigating the scale dependence of some classical or less classical statistical indicators that often vary as a power-law of the time (or spatial) resolution or lag. The exponents of such power-laws can therefore characterize a physical process over given range of scales. For instance, the approaches proposed by Kolmogorov (1941) for turbulence or by Hurst (1951) in hydrological science have led to a vast scientific literature.

Among various statistical tools that can be used to investigate scaling properties, spectral analysis offers a relatively simple and convenient way to study the distribution of energy across a wide range of temporal or spatial frequencies. In particular, power spectral densities have been used as a tool to investigate the temporal scaling properties of various hydrologic variables such as rainfall (Fraedrich and Larnder, 1993; Olsson, 1995 ; Verrier et al., 2011), river flows (Pandey et al., 1998) or soil moisture (Katul et al., 2007).

In the spectral sense, a time series is scaling if its power spectral density $E(f)$ is proportional to a power law of the form:

$$E(f) \sim f^{-\beta} \qquad \text{(Eq.1)}$$

where f is the frequency and ~ denotes equality within the limits of slowly varying factors that do not affect the main scaling behavior. (Eq. 1) is valid for frequencies f comprised between two limit frequencies defining the limits of the scaling range in which the scaling properties have been found. For some processes like rainfall, several distinct scaling ranges may be found in the series, with possible meteorological interpretation (e.g., Fraedrich and Larnder, 1993). In the case of soil moisture, Katul et al. (2007) used theoretical and empirical arguments to separate two ranges, one with a steep spectrum (behaving like $1/f^2$ spectrum or steeper) at high frequencies (equivalent to time scales from hours to about one hundred hours) and another one with a flatter spectrum at lower frequencies (i.e. larger time scales).

2.2 Multifractals and cascades

Multifractality may be viewed as a generalization of classical scaling properties to systems that do not exhibit a unique scaling law per scaling range but a whole set of scaling laws with specific parameters that nonlinearly depend on the order of statistical moments used in analysis (Schertzer et al., 2002). Physically, it is interesting to investigate different orders of statistical moments since they are representative of various levels of intensities of the process (e.g. moderate intensities vs. extreme intensities).

Let us denote $\lambda = T/\tau$ the resolution factor consisting of the ratio of the series time length T and a given analysis time scale τ (comprised between the time lag between two measurements and T). In the strict sense, a time series $\Phi(t)$ is said to be multifractal if its statistical moments of real positive orders q follow power-laws of the resolution λ:

$$\langle \Phi_\lambda^q \rangle \sim \lambda^{K(q)} \qquad \text{(Eq.2)}$$

In the previous equation, Φ_λ represents a low-resolution version of the original times series, obtained by direct aggregation over disjoint intervals of length $\tau = T/\lambda$. Other approaches could have been used for defining aggregated products (moving averages, wavelets…) but these approaches will not be considered in the following.

In theoretical terms, stochastic processes following (Eq. 2) may be built by iterative multiplicative procedures called multiplicative cascades (Schertzer et al., 2002). These procedures consist in a series of resolution refinements where a given coarse scale series is modulated by random multiplicative factors at each step (i.e. at each resolution refinement). Resolution refinements can be done by explicitly dividing coarse pixels in smaller subpixels, thus causing a discretization of the scales. Alternatively this construction can be extended to consider a continuum of scales, leading to continuous in scale multiplicative cascades (Schertzer and Lovejoy, 1997). For the latter, random multiplicative factors between two arbitrary scales should follow a log-infinitely divisible distribution.

In the general case described by (Eq. 2), the scaling exponent $K(q)$ is a convex function of the moment order q. However, the exact form of $K(q)$ is subject to additional constraints when taking into account the continuity of the scale space and the related constraints such as the distribution of random multiplicative factors described above. Based on these considerations, some authors proposed cascade models where the function $K(q)$ can be expressed in closed form. In particular, two-parameter models have been proposed by Schertzer and Lovejoy (1987) and by She and Levêque (1994).

In the following, the parameterization of the $K(q)$ function will be investigated with the help of the Universal Multifractal (UM) model proposed by Schertzer and Lovejoy (1987). The choice of this model was motivated by several factors such as its mathematical pertinence (the model is one of the natural attractors of the class of continuous in scale log-infinitely divisible cascades), its wide use in geophysical literature, and its physically interpretable parameterization.

In this framework, the function $K(q)$ is parameterized as follows:

$$K(q) = \frac{C_1}{\alpha - 1}(q^\alpha - q) \quad \text{(Eq. 3)}$$

C_1 is a dispersion parameter comprised in the interval [0,1] for time series. For instance $C_1 = 0$ would correspond to a homogeneous time series. Mathematically, C_1 is the fractal co-dimension associated to the set of points exceeding a specific threshold specifically related to the mean value of the field . The parameter α is an index of multifractality and belongs to the [0, 2] interval ($\alpha = 0$ is the pure monofractal case where $K(q)$ becomes linear while $\alpha = 2$ corresponds to log-normal cascades for which scaling exponents $K(q)$ vary in a quadratic way with q).

2.3 Fractionally integrated cascades

By construction, multiplicative cascades are potentially appropriate for modeling time series whose power spectrum follows a scaling law with a scaling exponent $\beta < 1$. More precisely the scaling exponent should follow the relationship $\beta = 1-K(2)$ where $K(2)$ is necessarily positive (see, e.g., Tessier et al., 1993, §3.b).

However, most geophysical variables are characterized by steeper power spectra ($\beta > 1$) in space and/or time domains. This is typically the case for variables closely related to turbulence (where β is generally close to 5/3 for both wind speed and passive scalars coherently with the predictions of Kolmogorov (1941), Obukhov (1949), and Corrsin (1951)), but also for many other variables, including topographic fields (Gagnon et al., 2006). Anticipating on Sect. 4, the subsequent analyses of SMOSMANIA soil moisture will show evidence of power spectra that are closer to $1/f^2$ behavior.

In the latter cases, multifractality can be investigated by testing the validity of (Eq. 2) for a derivative of the process, called the flux and denoted Φ. This derivative can be a fractional derivative of the original process. It is recalled that fractional derivative and integrations are useful notions of fractional calculus that extend classical definitions of derivatives and integrals to non integer orders (Loverro, 2004). These concepts are useful for modeling processes with various spectral scaling exponents, e.g. integrations can represent effects leading to steeper power spectra (Schertzer and Lovejoy, 1991, appendix B2; Gagnon et al., 2006). In the context of our study, the observable variable Y (e.g., soil moisture) is modeled as the fractional integration of order H of a multifractal flux Φ that follow Eq.2. Combined with UM cascades, this defines the Fractionally Integrated Flux (FIF) model (Schertzer and Lovejoy, 1987) which depends of the three parameters α, C_1, and H. When H is positive, its effect is that of a smoothing parameter. On the contrary, the case $H < 0$ corresponds to additional roughening effects. The case $H = 0$ corresponds to multiplicative cascades described in the previous paragraph (i.e. without any additional smoothing or roughening).

In practice, this parameter H may also be estimated by computing the first-order structure function $S(\Delta t)$ defined by the first-order absolute increments of the time series as a function of the time lag Δt:

$$S(\Delta t) \stackrel{\text{def}}{=} \langle |Y(t+\Delta t) - Y(t)| \rangle \quad \text{(Eq.4)}$$

In the case of a FIF model, $S(\Delta t)$ follows a scaling law similar to the one exhibited by fractional Brownian motions processes:

$$S(\Delta t) \sim \Delta t^{H} \quad \text{(Eq. 5)}$$

where ~ again means equality within the limits of slowly varying factors. It should be mentioned that the definitions above can be extended by using other definitions of fluctuations in time series. For instance, Lovejoy and Schertzer (2012) have proposed a variant based on the replacement of difference fluctuations used in Eq. 4 by Haar fluctuations. Interestingly, such variants may differ from each other in terms of range of validity of H estimates. For instance, structure functions estimates based on Eq. 4 will allow the retrieval of H only when $0 < H < 1$. The use of Haar fluctuations can lead to correct estimates on a wider range of H values ($-1 < H < 1$). In the rest of the paper, analyses will nevertheless be based on the more classical structure functions defined by (Eq. 4). This is not a limitation here since H estimates will be found near the middle of the [0, 1] interval (see section 6.2).

The value of H directly affects the distribution of energy across scales: namely, a higher value of H implies a steeper spectrum. For a FIF series, both values are related by $\beta = 1-K(2)+ 2H$ (Tessier et al., 1993). Note that for a monofractal signal such as a fractional Brownian motion (characterized by a unique scaling exponent H), a more or less similar relationship ($\beta = 1 + 2H$) still holds. The case of FIF processes differs from the fBm case by the multifractal correction term $K(2)$.

2.4 Multiscale entropy

Other signatures of scale-invariance may be found by using analysis methods more closely related to information theory. For instance, the notion of information dimension has been defined to characterize the density of points in fractal geometric sets and strange attractors (e.g., Hentschel and Procaccia, 1983; Farmer et al., 1983). Zhang (1991) suggested computing Shannon entropies of coarse-grained time series as a prerequisite to define a complexity measure of a signal. A similar approach has been proposed by Costa et al. (2002, 2003, 2005) in the context of the analysis of biological signals. Their approach, called Multiscale Entropy (MSE) is based on the estimation of the sample entropy (SampEn) (Richman and Moorman, 2000) applied on time series that are coarse-grained at various time resolutions. The sample entropy provides an approximation of the entropy information of any discrete time series $y[i]$ of length N by computing the conditional probability that two similar sequences of m consecutive points will remain similar when considering extended sequences of m+1 points.

If $u_m[i]$ denotes a sequence (vector) of *m* points starting at index *i*, i.e. $u_m[i] = \{y[i], \ldots, y[i+m-1]\}$, and *d* is a given distance between vectors (here taken as the maximal absolute distance between their components), then we may define the probability of similarity between two different vectors with respect to a threshold *T*:

$$A(m,T,N) = \Pr(\, d(u_m[i], u_m[j]) \ \leq T) \qquad (j \neq i) \qquad (\text{Eq. } 6)$$

Then the sample entropy may be computed by estimating the negative logarithm of the conditional probability that two matching vectors of length *m* will still match while taking into account an additional point within all vectors (Costa et al., 2005):

$$S_E(m,T,N) = -ln\left(\frac{A(m+1,T,N)}{A(m,T,n)}\right) \qquad (\text{Eq. } 7)$$

Due to the negative logarithm, the sample entropy tends to increase when “unexpected” changes in the series tend to occur, i.e. when they are less repetitive and contain more information. In the following, the parameters *m* and *T* will be fixed to values close to those used in the literature, i.e. *m* = 2 and *T* taken as 15% of the standard deviation of the time series *y*.

Within this context, the Multiscale Entropy is a procedure consisting at estimating the sample entropy not only from given a data time series $Y[i]$ but also from coarse-grained time series $Y^{(\tau)}[i]$ that may be estimated by averaging *Y* over non-overlapping windows of length τ. This provides an entropy estimate MSE(τ) that depends on the time resolution τ.

Recent results tend to prove that scale invariance has a specific signature on the Multiscale Entropy: as recalled by Nogueira (2017), MSE(τ) should scale as a power-law with exponents closely related with the spectral slope., i.e.

$$MSE(\tau) \sim \tau^{H'} \qquad (\text{Eq. } 8)$$

This has been verified empirically in the case of colored noise/fractional Brownian motion (fBm) time series (Courtiol et al., 2016). Analytical arguments based on fBm theory have also been proposed by Gao et al. (2015) to understand this relationship. These authors also confirmed their findings on empirical studies of biological signals.

Nogueira (2017) compared the scaling laws of power spectra and MSE approach for both geophysical data (near-surface wind) and synthetic data (based on monofractal fBm series). In the case of monofractal fBm signals, the results were tending to confirm that the MSE scaling exponent *H’* should be identical to the scaling exponent *H* determined by the first-order structure function. On the contrary, the case of multifractal signals has not been explicitly analyzed. It may be noticed that Nogueira's empirical results on turbulent (i.e., likely multifractal) wind processes suggest that a scaling law if the form of Eq. 8 could still hold for multifractal signals.

In the following, both MSE tools and multifractal analysis tools will be applied to the same SMOSMANIA surface soil moisture time series. This will provide two types of multiscale information that could eventually be compared.

3 Data sets

SMOSMANIA consists of a network of about 20 measurement stations distributed across Southwestern and Southeastern France in grassland and agricultural areas (Calvet et al., 2007; Albergel et al., 2010, 2011). This network has been set up in relation with the much broader HyMeX campaign (http://www.hymex.org) which was mainly devoted to the monitoring and modeling of water cycle within the Mediterranean region. The SMOSMANIA probes are located at existing operational Météo-France weather stations (RADOME network). The average distance between two SMOSMANIA stations is of the order of 45 km (Albergel et al., 2010). These locations may be viewed at ISMN website at the following address: www.geo.tuwien.ac.at/insitu/data_viewer/ISMN.php. All stations are located at places with a fallow vegetation cover.

The SMOSMANIA network provides operational measurements of volumetric soil moisture and soil temperatures at various depths. Concerning the former, soil moisture is estimated on a hourly basis with the help of Thetaprobe sensors based on a capacitive technology. Measurements are available at four references depths ranging from 5 cm to 30 cm. All the time series may be downloaded for free at the International Soil Moisture Network (ISMN) page (http://ismn.geo.tuwien.ac.at/data-access/). For more information about ISMN, the reader is also referred to the presentation by Dorigo et al. (2011).

The present study is focused on time series located in Southwestern France, i.e. on time series of soil moisture collected at 12 places reported in Table 1. Since scaling-related analyses must generally rely on data that have a small number of missing data, time series presenting long missing periods of several dozens of days have been discarded. We therefore restricted the study to nine of the twelve initial series (discarded series are marked with a star in Table 1). All remaining missing data have been replaced by linear interpolation.

Several differences between locations should be noted. For instance, Urgons, Sabres, and Créon d'Armagnac are located closer to the Atlantic ocean and therefore are subject to a more oceanic climate. They also differ from most of the other stations by a different soil texture with a much larger sand proportion. Stations that are closer to the Mediterranean Sea (Narbonne, Lézignan-Corbières) typically have a silt loam texture. Finally, stations that are distant from both seas tend also to have the largest clay fraction (Condom, Peyrusse Grande, Lahas). We can notice that all stations (except Mouthoumet station) are located at low altitudes.

The present study is focused on the 2007-2014 period that covers most of the available time series from ISMN. Thus, all soil moisture measurements comprised between 2007/01/07 6:00 and 2015/01/01 0:00 (local time) have been selected in order to cover approximately 8 years. Measurements before 2007/01/07 were only available at a few stations and thus were discarded. Since all sensors provide measurements on an hourly basis, all selected time series have about 70,000 data points which provides the possibility of investigating potential scaling properties over four orders of magnitude in scale.

Finally, some data at the beginning of the data series have been removed in order to reduce all the time series to 65536 measurements points each. All the retained series still cover the same dates, ending on 2015/01/01 0:00. The purpose of this restriction is to work with 2^n length time series (here n = 16) which is preferable for technical reasons. Indeed, multifractal analysis requires the estimation of statistical moments at different aggregated resolutions and the use of a dyadic cascade (i.e. 2^i resolutions with integer i) is very convenient for this. Moreover, FFT-based spectral analysis techniques are also faster when applied to series with 2^n data points.

4 Spectral analysis of SMOSMANIA series

4.1 Surface soil moisture data (5 cm depth)

Spectral analysis has been carried out on the data set of soil moistures measured at 5 cm depth in order to identify scaling properties and possible scaling ranges. Since scaling properties generally take the form of a power-law spectrum, i.e. $E(f) \sim f^{-\beta}$, the results are presented in logarithmic coordinates. In such a graph, scaling laws should indeed appear as linear. However, this representation may have less desirable counterparts when analyzing long time series. In particular, this usually results in a much denser sampling of frequencies near the high frequencies and often in a less readable graphic representation. To avoid these problems, an average of the spectra over equally spaced logarithmic bins (of length 0.02 here) was performed.

The power spectra of the nine selected series are shown on Figure 1. The figure is presented in logarithmic coordinates. In order to make it more readable, the spectra are translated upwards from one station to the next one. The spectrum of the Condom series is the only one that has not been vertically translated. Time scale tick labels are displayed on the horizontal axis (i.e. high frequencies are still on the right of the figure but the horizontal graduations specify the time scale equivalent to this frequency, i.e. $\tau = 1/f$).

The main feature exhibited by the spectra on Figure 1 is the presence of scaling laws over a large scale range covering a large range of scales. All spectra seem nevertheless slightly steeper at the high frequencies than at low frequencies. A more oscillatory behavior at low frequencies (e.g. time scales larger than several thousands of days) may be noticed. This feature is probably related to the coarser sampling of frequencies when analyzing large scale structures over time series that is not much longer than these structures.

It may also be noticed that all spectra appear roughly parallel to each other which suggests that all spectra should have very similar scaling laws with exponents β that are not expected to vary much. This may be checked by calculating these scaling exponents.

While the spectra look scaling over three orders of magnitude at first glance, several additional factors must be taken into account to determine the scale range considered in the fits: (i) the low-frequency part of the spectrum has a poorer sampling and is less robustly estimated, (ii) the application of a segmentation algorithm (D'Errico, 2017) has been used to identify possible transitions between ranges with different spectral exponents β, but failed to notice very significant transitions, (iii) however, some spectral estimations (for instance at Lahas station) exhibit a very local drop at time scales of the order of 1000-3000 h, (iv) the retained fit range must permit linear regressions with a good coefficient of determination, for example $R^2 > 0.98$.

Taking these elements into account and also anticipating on Sect. 5 where a narrower scaling range will be found, the estimation of scaling exponents has been limited to the range of scales 1000h – 1h. The linear regressions are shown on Figure 1 and the scaling coefficients β are reported in Table 2 (for the nine soil moisture time series collected at depth 5 cm). It may be noticed that this choice permits one to obtain a very good coefficient of determination for each of the nine spectra presented. All spectral slopes β are found within or very close to the range [1.9, 2] and thus are very similar to each other when considering that each exponent is given with an uncertainty of ±0.04. This confirms the apparent parallelism of the spectra on the figure.

4.2 Other depths

By repeating the above procedure for the three other depths, similar results were obtained with scaling holding to a good approximation for scales smaller than 1000 h (all error bars Δβ were found smaller than 0.04 for a linear fit within this range). For all time series, the surface (5 cm) data spectrum remains above the other spectra, meaning that the surface series contains more energy (in the signal processing sense) than the other ones. Physically, this is also coherent with the greater variability amplitude of soil moisture at the surface due to the meteorological forcing.

However, significant differences have been found between stations with typical cases illustrated on Figures 2a and 2b. At Peyrusse Grande station (Fig. 2a), the spectra are close to each other and the spectral slopes do not change considerably with depth (here from 1.93 to 2.08) while at Montaut the spectra are clearly distinct with different spectral slopes (ranging from 1.97 to 2.35). It may be noted that the spectra displayed on Figure 2 do not include any vertical shifts between spectra.

The spectral slopes β estimated for all stations at all considered depths are summarized on Figure 3. The estimates of β are represented on the vertical axis while the stations names are distributed on the abscissa axis (the stations have been sorted from the most western position to the most eastern position). More precisely, the abscissa axis refers to the three first letters of the names of the stations. Error bars are omitted but are of the order of ±0.03 or 0.04 for all estimates.

As illustrated on Figure 2 and Figure 3, it seems that the spectral slope tends to increase as we consider deeper layers. However, β estimates become more variable across stations as the depth increases. This could possibly be related to the differences in subsurface processes and soil texture, the latter being heterogeneous across the stations.

While similar studies in the region of interest do not seem to be reported in the literature, several published studies may help to put our findings in perspective. In the space domain, lower scaling exponents are generally reported. For instance, Pelletier et al. (1997) found a value of β = 1.8, while a value closer to 1.2 might be deduced from the findings presented by Kim and Barros (2002a), based on remote sensing data. More recently, Neuhauser et al. (2018) reported a spectral exponent closer to 1.0 at spatial scales > 40 km based on SMOS data.

In the time domain, higher estimates of β have been reported by Katul et al. (2007) based on measurements of soil moisture in a more subtropical eastern US region (Durham, NC). These authors considered an eight-year long time series of integrated (0-30 cm) soil moisture. They found a steep scaling β = 2.75 in the scale range 90 h – 1h and a much flatter spectrum at larger scales. Interestingly, they also proposed a simplified physical model to show that soil moisture time series may behave as a time integration of precipitation time series at relatively small time scales (at least in first approximation). Since power spectra of precipitation data are either flat or decrease in a scaling way (i.e. f^{-a} where $a > 0$, cf. Fraedrich and Larnder, 1993), the expected spectrum of soil moisture could be of the form f^{2-a}, which was verified in their case. The results obtained by Katul et al. (2007) therefore suggest that it is not surprising that soil moisture has a steeper scaling in the time domain than in the space domain, due to this time integration effect. However, in the present study estimates of β are found closer to 2.0, i.e. a red-noise like scaling. In this sense, our results may differ from those of Katul et al. (2007) since the model proposed by the latter authors does not seem compatible in practice with values of β smaller than 2.

5 Multifractal analysis

5.1 Surface soil moisture data (5 cm depth)

Results of the previous section show that soil moisture power spectra estimated above are rather steep (similar to a f^{-2} red-noise). This usually means that the series cannot be directly described by a multifractal multiplicative cascade which requires β < 1. However, as explained in Section 2.3, it is possible to check whether a multifractal cascade structure may describe some derivative (or integration) of the process. Fractionally integrated stochastic processes (e.g. fractional Brownian motions, fractionally integrated flux…) are models that may be appropriate for scaling processes with steeper spectral slopes. Therefore, a possible way to investigate multifractality within the series is to consider a "flux" estimated from a derivative of the time series and to test whether the moments of this flux follow a multifractal law analogous to that described in Section 2.2 (Eq. 2).

In the following, the fluxes Φ are estimated at 1h resolution by taking the absolute value of the finite difference derivative of the 5cm moisture series, following the process originally described by Lavallée et al. (1991, 1993). For each series, the flux is aggregated over non-overlapping intervals of length $\tau = 2^{i}\tau_0$ using a dyadic cascade approach (i.e. at each step the resolution ratio $\lambda = T/\tau$ is divided by a factor two and the data are aggregated on successive couples of points). This leads to an ensemble of aggregated fluxes series $\Phi_\lambda(t_i)$ indexed by the resolution $\lambda = 2^j$ for j = 0, 1, …, 16 (each aggregated series thus containing λ data points).

Then the empirical moments are used as an estimate of the (unknown) statistical moments. For each series, and for each chosen moment order q, the aggregated fluxes are elevated to power q and averaged over the whole series length. The computation is done for all averaging resolutions $\lambda = 2^j$ (j = 0,1,…, 16) and for various orders q comprised between 0 and 2.5 (with a spacing of 0.1 between two successive orders). This provides the empirical moments $M(\lambda, q)$ that approximate the statistical moments $\langle \Phi_\lambda^q \rangle$, the statistical average being replaced by the empirical average. This procedure corresponds to the Trace Moment approach presented by Tessier et al. (1993).

The empirical moments are represented in logarithmic coordinates as a function of the resolution λ. The process is repeated for each series. The result is displayed in a larger figure for the case of Peyrusse Grande data, and in a composite figure for other stations (see Figures 4 and 5).

Figure 4 may be read as follows. First, each curve is associated to one specific moment order. The higher moment orders $q > 1$ are associated with the upper, increasing curves on the figure, while the slightly decreasing curves are associated to orders q such that $0 < q < 1$. Similarly to Figure 1, finer resolutions are located on the right of Figure 4.

At the coarsest time scales, typically > 1000 h, the curves are undistinguishable meaning that no significant multiscaling may be found. However, moments are much more variable towards finer resolutions. Log-log linear behavior is found to a good approximation within the range of resolutions comprised between 128 h and 1 h (green fit lines). Since the figure is in logarithmic coordinates, each regression is representative of Eq. 2 for a fixed order of moment q and its slope corresponds to the scaling exponent $K(q)$.

Comparable figures are found for the eight others time series with very similar scaling ranges (Figure 5). Thus, and in order to facilitate the comparison between the different series, it has been chosen to perform the regression over the same scaling range (128 h – 1 h). It can be noted that this range is smaller than the one observed on power spectra presented in the previous section.

Based on Figure 4, we also remark that all linear regressions are convergent towards a point while being extrapolated towards coarser resolutions. The abscissa of this point may correspond to the "external scale" (Lovejoy et al., 2008) at which the multifractal cascade is initiated. For the nine time series, the exact position of the external scale may vary a bit but is comprised in the range 200-600 hours. For most of the time series, the external scale would be close to 200-300 h, but for some of them higher values seem obtainable (e.g., Urgons, Narbonne, or Créon d'Armagnac). For the latter station, the external scale seems indeed closer to 600 h. Due to the uncertainty of this estimate, it is not possible to clearly tell if the latter difference is really significant and related to meteorological forcing. Nevertheless, the position of the external scale is plausibly related to the weather/macroweather transition scale that has been evidenced for numerous atmospheric fields (Lovejoy et al., 2013; de Lima and Lovejoy, 2015). The transition between the weather and macroweather regimes occurs at the lifetime of planetary meteorological structures, i.e. at time scales of the order of a couple of weeks. For meteorological variables, the transition separates scaling regime respectively characterized by a small intermittency (i.e. large-scale/macroweather) and a stronger (multifractal) intermittency at smaller scales (i.e. weather regime).

As explained above, the slopes of the green lines on Figure 4 provide the estimates of the moment scaling function *K*(*q*) for the orders *q* that have been used in previous computations. The graph of the estimated *K*(*q*) function at Peyrusse Grande station is provided on Figure 6. The round dots correspond to the empirical estimates. We may notice that the values of *K*(*q*) are also given for higher moment orders (up to 3.0) that have not been represented on Fig. 4 for readability purposes.

As expected, the *K*(*q*) estimates are distributed along a convex curve. The latter may then be fitted by the two-parameter universal form recalled in Section 3. The green curve is obtained by nonlinear optimization on the interval defined by $q \in [0\,, 2.5]$. More precisely, the Nelder-Mead method is used to find the couple of parameters that minimizes the (quadratic) distance between fixed *K*(*q*) estimates and the theoretical values predicted by (Eq. 3). In this case, the universal parameters estimates for Peyrusse Grande station are $C_1 = 0.28$ and $\alpha = 1.51$.

For other stations, more or less similar graphs may be obtained but some variability still exists in both estimates of α and C_1 (Fig. 9). All the different *K*(*q*) function estimates were fitted within the interval $[0\,, 2.5]$ (see Figure 5). The obtained parameters are reported in Table 3.

As shown on Table 3, some variability may be found within parameter estimates. Nevertheless, C_1 remains always close to 0.25-0.3 and the observed variability does not seem related with the positions of the stations and/or soil texture. Such estimates are significantly larger than the values (closer to 0.1 or even less) reported for other geophysical fields (e.g., Lovejoy and Schertzer, 2013). However, some studies report large (> 0.3) estimates in the case of rainfall (e.g., Lovejoy, Schertzer et al., 2008), at least at time scales larger than 1 h (Verrier et al., 2011). Thus, the relatively high value of C_1 that has been observed in this study for soil moisture could be a consequence of the large intermittency of the rainfall process. Concerning the index of multifractality α, most estimates are found within the range 1.6-1.8. In this aspect, the stations of Créon d'Armagnac and Urgons seem to differ significantly from the others with much lower α estimates closer to 1.3-1.4. Interestingly, these stations are relatively close to each other (about 55 km) and both located in the French department of Landes, at the most western part of the region covered by SMOSMANIA, i.e. closer to the Atlantic Ocean and with significantly more sandy soil texture. This could suggest a possible impact of these features on α. However, the parameter α characterizes the degree of nonlinearity of the *K*(*q*) curve and is known to be more difficult to estimate than C_1. This could also explain part of the observed difference despite the relative homogeneity of α estimates for the other stations.

5.2 Other depths

By repeating the previous analysis to other depths, a similar multifractal scaling was found in the range 128 h – 1 h for all stations. This is illustrated on Figure 8 where moments of Peyrusse Grande (10, 20, 30 cm) data follow a scaling law that could be extrapolated to external scales of the order of several hundreds of hours. From the slopes of the green lines, scaling exponents $K(q)$ may be computed and then plotted on Figure 8 (bottom right). On this figure, each color is associated to one depth (note that 5 cm depth estimates are also plotted on the same graph). While the different curves globally follow the same shape, they differ significantly from each other for low and high moment orders. In this case, high-order moments are higher for 10 cm depth data than for other data, while 20 cm depth data differ from the others for low moment orders. These differences affect both estimates of multifractal parameters, which can be checked by comparing the couples (α, C_1) at depths 5 cm and 20 cm. Indeed, the latter are respectively equal to (1.51, 0.28) and (0.79, 0.40). Part of the change may be explained by the partial "linearization" of the $K(q)$ curve as the depth increases (the limit case of linearity can theoretically be attained at α = 0, i.e. monofractality case).

For all time series, the parameters α and C_1 have been estimated at the different depths. The results are summarized on Figures 9a and 9b where estimates are given as a "function" of the station (once again, stations are sorted from the most western to the most eastern and are identified by their first three letters). As deeper data are considered, smaller values of α and larger values of C_1 are systematically obtained, with a globally larger variability from one station to one another. Similar to Fig. 8, this change seems to be related to a less pronounced convexity of the $K(q)$ curves as depth increases.

We may conclude that soil moisture at these depths still follows multifractal properties but with different $K(q)$ scaling exponents, especially at low and high order moments. This is illustrated by a change in multifractal parameter estimates that is noticeable when compared to the relative homogeneity of the parameters for 5 cm depth data across different stations. A possible explanation could reside in the impact of soil texture on soil moisture at the deeper layers. For instance, subsurface processes could cause a change of the scaling of some moment orders, this change propagating to the multifractal parameters.

6 Multiscale entropy properties

6.1 MSE analysis

The nine surface (5 cm depth) soil moisture time series are now analyzed within the MSE framework. For each series, sample entropy is estimated at various coarse resolution time series obtained by the means of averages performed over non-overlapping intervals of various durations τ chosen between 1 h, i.e. the finest resolution available, and 690 h. We cannot degrade the time series to coarser resolutions since the sample entropy calculation can only be performed over coarse time series containing at least 100 points (Nogueira, 2017). The estimated entropies are represented in logarithmic coordinates on Figure 10 for the different time series. Once again, MSE curves are regularly shifted upwards to make the figure more readable. MSE curves are steeper at lower time scales and a bit flatter at larger scales. The segmentation tool proposed by J. D'Errico (2017) was used to estimate the position of the transition between the two behaviors, with a result close to 30 h. Due to the better sampling of the MSE on the right of the figure, only time scales within the range 650 h – 30h have been considered for fitting. The exponents *H'* are determined by linear regressions over this interval of time scales. The values of *H'* estimates and error bars may be found in Table 4. Estimates are comprised between 0.31 and 0.66 for a mean value of *H'* = 0.43 for all time series. All the regressions have a very good coefficient of determination except in the case of the Mouthoumet station.

Despite the narrower scale range, the results are partially coherent with the findings previously obtained by spectral analysis, with often similar scaling exponents across stations (see Table 2). Once again, all time series have rather similar scaling properties which could be related to the sampling strategies (all sensors being located in grassland on flat areas). Nevertheless, it could be noted that the dispersion of the values of *H'* is greater than the dispersion of spectral slopes. This dispersion is nevertheless probably not representative of a better sensitivity of MSE to local differences: indeed, *H'* is estimated over a significantly narrower scale range than β which could lead to more dispersion in the estimates.

Furthermore, the soil moisture series collected at 10 cm, 20 cm and 30 cm depths have been analyzed in a similar way. The scaling exponents *H'* obtained by fitting the MSE curves are displayed on Figure 11. All these exponents have been obtained by linear fits on the log-log graph of MSE(τ) for time scales in the range 30h – 650 h (all linear regressions had an R^2 greater than 0.94 except in the case of Peyrusse Grande where the fits are poorer). Figure 11 also confirms that the scaling exponents may depend on depth. Coherently with what was reported on Figure 3, the scaling seems in general a bit steeper at greater depths.

The results of this section confirm that the scaling properties of soil moisture may be retrieved not only in terms of spectra and moments, but also in terms of information content. This was expectable since the signal information (occurrence of unexpected structures) is of course strongly constrained by the probability distribution of the signal at various resolutions. Nevertheless, this result shows that multiscale entropy scaling can be found in non-biological natural signals, consistently with the findings by Nogueira (2017). Additionally, our results show that MSE scaling may be found in natural signals that follow multifractal statistics. This could extend the findings of the literature that mainly focuses on monofractal Brownian processes or natural processes assimilated to the former ones (e.g. Gao et al., 2015).

Complementarily, we may investigate which degree of redundancy may exist between the MSE approach and the structure function approach, i.e. to check if they estimate the same scaling properties or not. Indeed, first-order structure functions can be used to estimate the third parameter *H* of the FIF model (cf. Section 2.3). In the case of our dataset, is *H* indeed close to the MSE scaling parameter obtained above?

6.2 Comparison with first order structure functions

In order to investigate this issue, the first-order structure functions (defined by Eq. 4) have been estimated based on the surface soil moisture data from the nine stations. The structure functions are displayed on Figure 12, where they are regularly shifted in the vertical direction to improve readability. It should be noted that on Figure 12, the large time increments are on the right of the figure. Very small and very large time increments are not taken into account as they might be affected by sampling limitations. On the middle of the Figure 12, a scaling regime may be identified for $30\ h \leq \Delta t \leq 1000\ h$. This regime is representative of a scaling behavior of the form given by Eq. 5. In order to make the comparison with Sect. 6.1 easier, the linear fit range was restricted to $30\ h \leq \Delta t \leq 650\ h$. Good scaling results are obtained, with an very small error bar on the slope estimate ($\Delta H \approx \pm 0.01$ or smaller). The scaling exponent does not vary much from one series to one another, the mean value of *H* being equal to *H* = 0.41 (see values in Table 5).

We may now compare the estimates of *H* and *H'* obtained for the different series. Figure 13 displays *H'* as a function of *H* for the different time series. For most stations, estimates of *H* and *H'* are very similar despite some differences larger than the regressions error bars. However, significant differences were found for two stations (Narbonne and Savenès) where the *H*' estimates are much larger than their structure function counterparts. It remains unclear if this is due to greater uncertainties in the estimates obtained by the MSE approach and/or an ability of the latter method to catch specific features at some stations. This issue could be investigated in future studies since MSE and structure function approaches may perform differently in the estimation of Hurst-like scaling parameters.

While the detailed comparison of the two methods still requires additional theoretical work, we can already notice that each method has qualitatively identifiable practical advantages and drawbacks. Namely, classical structure functions are more easy to use to analyze a large scale range but do not have direct interpretation in terms of signal information. Additionally, they cannot estimate negative scaling exponents (unless modified variants based on wavelets are used, e.g., Lovejoy and Schertzer, 2012). Meanwhile, MSE algorithms are appropriate for information and complexity estimation but they are applicable over a relatively limited scale range due to computational constraints (Nogueira, 2017). The MSE framework also provides equations that seem more difficult to relate analytically to equations such as those governing the statistics of multifractal cascades for non-unity orders of statistics (Eq. 2). It could be interesting to try to investigate possible links with other theoretical notions such as the information dimension, which contains both scaling and (Shannon) entropy characterization. The latter point is left as a perspective in this work. However, a better understanding of the possible relationship between multifractal scaling and MSE scaling can already be achieved with the help of numerical tests. This is the subject of the next section.

7 Expected relationship between *H'* and multifractal parameters

7.1 Numerical experiments

The analysis presented in Section 6 was aimed to test if H and H' estimates could have close values in the empirical case of the study. While the hypothesis $H \approx H'$ has been tested numerically by Nogueira (2017) in the case of fractional Brownian motion processes where the structure function H is the unique scaling parameter, the extension to the case of multifractal processes has not yet been investigated by theoretical or numerical approaches (at least to the author's knowledge). Multifractal processes differ from fractional Brownian motions by the existence of more nonlinear properties that are characterized by the parameters C_1 and α defined above. A priori, there is no theoretical reason to rule out a possible effect of C_1 and α on the MSE scaling parameter. Therefore, we might look for a possible functional relationship of the form $H' = f(H, C_1, \alpha)$. While it is still unknown if this function f can be defined in closed form, numerical tests can be performed to check if there is a systematic dependency of H' on the three multifractal parameters.

In the following, numerical tests are presented based on the multifractal simulation techniques of FIF processes described by (Pecknold et al., 1993; Schertzer and Lovejoy, 2002; Macor, 2007; Verrier, 2011). The main steps are the following: (i) generation of a unit extremal Lévy-stable noise (with an asymmetry parameter equal to -1 and a stability parameter α identical to the multifractal α defined above); (ii) multiplication by a (normalizing) multiplicative constant $\sigma = \left(\frac{C_1}{\alpha-1}\right)^{1/\alpha}$; (iii) Convolution by a kernel proportional to $|t|^{-\frac{D}{\alpha}}$ where D is the embedding space dimension (i.e. $D = 1$ for time series); (iv) Exponentiation; (v) fractional integration of order H. Step (i) above is performed by applying the procedure described by Chambers et al. (1976) to a couple of independent simple random variables at each data point. It is worth noting the procedure allows to store numerical realizations of these two simple "input" variables U and E (with uniform and exponential distributions respectively, cf. Pecknold et al., 1993, § 3) and then to repeat the five-step procedure with different sets of parameters (H, C_1, α). Therefore, it is very easy to test different sets of parameters on the same probabilistic events (i.e. numerical realizations).

Numerical tests have been implemented in the following way. Twenty independent realizations of couples of U and E time series are first generated in order to build the experiment on twenty different probabilistic events. Then, the procedure of simulation is applied for various sets of multifractal parameters (H, C_1, α) – in other words 20 synthetic multifractal time series are obtained for each set of parameters but the 20 random realizations used to generate the series are the same for all sets. Since synthetic multifractal time series can have numerical discrepancies at the highest frequencies, it has been chosen to perform all numerical simulations based on time series of 2^{18} points and then to average each of them over a series of disjoint intervals of 16 points. This procedure provides 20 time series of 2^{14} = 16384 points for each set of multifractal parameters.

In a second step, MSE analysis is applied to each individual time series and then the MSE(τ) function is averaged over the 20 individual realizations available for each set of multifractal parameters. The H' exponent is then estimated *from the averaged MSE(τ)* by performing a linear regression in log-log coordinates over the whole range of available scales (i.e. from 1 to 163 data points since sample entropy needs 100 data points to be computed).

7.2 Results

Examples of MSEs estimated from individual series are presented in log-log coordinates on Figures 14 and 15. Figure 14 shows the MSE(τ) obtained for a single random realization with $\alpha = 2$ and $C_1 = 0.05$. The blue curve is obtained when $H = 0$ and the green curve when H has been fixed to 0.4. It may be noticed that the effect of the fractional integration (i.e. transition from the blue to the green curve) changes both the height and the slope of the MSE(τ) function. In this individual case, the hypothesis $H' \approx H$ seems to hold when 0.4, but a moderate scaling is found in the $H = 0$. Figure 15 illustrate the case where the parameter C_1 changes (while $\alpha = 2$ and $H = 0$) based on a different individual realization. The increase of C_1 leads to a drastic decrease of the entropy and seems also to increase the slope H' of the MSE curve.

These conclusions are globally confirmed when considering the H' estimates obtained from the averaged MSEs (Figs. 16-17). Figure 16 shows the H' estimate as a function of H, with variable C_1 while α is fixed to 2. On the figure, each curve corresponds to one value of C_1 comprised between 0.05 (continuous blue curve) and 0.55 (dashed green curve) with a spacing of 0.10. H is sampled in the range [0, 0.7] with a spacing of 0.10. The first bisectrix is represented as a dashed black line. For all curves, H' increases with H but does not follow the bisectrix (except when C_1 is very small). When $H > 0.5$, all curves tends to get relatively close to each other meaning that when H is sufficiently high, the influence of C_1 on H' is relatively small. On the contrary, when $H < 0.4$, the influence can become quite large with a systematic increase of H' with C_1 (confirming the observation of Figure 15). In the case of a non integrated multiplicative cascade ($H = 0$), this can lead to an H' estimate varying within the range [0.1; 0.3] depending on the C_1 value. Regression error bars on H' estimated from the average MSE(τ) functions are not represented because they are very small (inferior to 0.01).

The possible influence of the α parameter (coupled with H) is presented on Figure 17, where H' is represented as a function of H, with one curve for one value of α (C_1 being fixed to 0.25). The parameter α has been chosen in the interval [1.5, 2] with a spacing of 0.1 (i.e., values usually encountered in geophysics, and also reported in this study). Again, H' is an increasing function of H for all curves which also remain above the first bisectrix. However, H' is a decreasing function of α such that the relationship between H' and H tends to become closer to the first bisectrix when $\alpha = 2$. We may notice that the dependency of H' on α is very limited for high values of α ($\alpha > 1.7$) but becomes more pronounced for smaller values. Finally, we may again notice that for high values of H, all curves become close to the first bisectrix and increasingly undistinguishable from each other (e.g., $H = 0.7$).

These numerical results show that the relationship between multifractal parameters and the MSE scaling properties is more complex than originally anticipated and that a dependency on the three multifractal parameters should be expected in the general case. However, we may distinguish two basic cases:

- For relatively high values of H (> 0.4-0.5), the relationship $H \approx H'$ might still provide a useful work assumption since our results suggest that the fractional integration washes out the possible effects of the multifractal parameters α and C_1. In this case, the MSE scaling properties of a multifractal process are expectedly close to those of a fractional Brownian motion which have been investigated by Nogueira (2017).
- For lower values of H, and in particular in the case of a non-integrated multiplicative cascade ($H = 0$), the effect of α and C_1 is visible and results in a MSE scaling exponent that is higher than H (i.e. $H' = H + g(H, C_1, \alpha)$). The positive offset modeled by the function g is higher when C_1 increases or when α becomes significantly smaller than 2. Interestingly, the offset becomes very small when C_1 takes small values, which illustrates that multifractal intermittency plays an important role in the difference $H'-H$.

While more exhaustive numerical tests and theoretical work remain to be done to quantify and understand the relationships between multifractal parameters and observed MSE scaling laws, some qualitative arguments may help to interpret the present observations. First, the effect of the fractional integration included in the FIF model is similar to a (scaling) low-pass filter that significantly attenuates the variability at the smallest scales. It is therefore expectable that a fractionally integrated signal ($H > 0$) possesses more entropy at coarse resolutions than at fine resolutions. This is obvious on Figure 14 where we see that the effect of H is to strongly reduce entropy estimates at small scales (i.e. on the left part of Fig. 14). Moreover, as already noted on Figure 15, high C_1

parameter values also contribute to strongly reduce entropy. This could seem a bit paradoxical since C_1 is known as an intermittency/heterogeneity parameter. However, multifractal processes with high C_1 correspond to processes that exhibit slow variations most of the time, while most of the variance is due to very strong and sparse peaks (e.g., fig. 10 in Pecknold et al., 1993). In this case, sample entropies tend to decrease since repetitive patterns are (or seem) more frequent due to the existence of wide areas with small variations. This effect is even more pronounced due to the increased standard deviation of the process when C_1 is large due to the contribution of extreme peaks. Indeed, since the sample entropy builds its similarity criterion by using the standard deviation of the series (see Eq. 6), it classifies events as similar more easily when large standard deviation and C_1 are involved. We can notice that the decrease of entropy is expectably stronger at small scales where peaks are both very intense and cover a very small fraction of the time.

7.3 Application to SMOSMANIA empirical parameters

Finally, we may come back to the results of Section 6 since we have just demonstrated that the initial hypothesis $H \approx H'$ may be too simplistic for multifractal processes in some situations. By reporting the parameters (H, C_1, α) estimated in Sections 5 and 6.2 to the graph presented on Figure 17, we obtain an expected parameter H' between 0.4 and 0.5. However, the empirical H' estimates found in Section 6.1 ($\approx$ 0.40) are less coherent with this expected parameter ($H' \approx 0.47$-0.48 for multifractal parameters $\alpha = 1.7$, $C_1 = 0.25$, $H = 0.40$) than the one resulting from the naive $H \approx H'$ hypothesis. Beyond possible estimation uncertainties, a plausible explanation for this observation is the fact that the multifractal parameters C_1 and α are expected to be valid in the range of scales 128h – 1 h, while H and H' are valid in the range 650 h – 30 h. At scales larger than 128 h (i.e., beginning of the “macroweather” regime), the flux moments have much slower variation with scale (Figs. 4-5), which is equivalent to a strong decrease of the C_1 parameter. This could explain why the empirical estimates of H' are close to the structure function exponents since it is what is expected for low values of C_1 (see Figure 16, continuous blue curve), especially when H is still relatively large (0.4 in this case).

8 Conclusions

Like other geophysical processes, soil moisture is strongly variable over a rather wide range of time (and space) scales. Some previous literature papers advocated the existence of scaling and fractal properties over various ranges of scales. In this study, 8-year time series of surface soil moisture have been analyzed with the help of various multiscale analysis tools in order to investigate the existence of scaling laws. The twelve sensors are located in the same area of about 300 x 200 km² in southwestern France and the average distance between stations is of the order of a few dozens of kilometers. For nine of these stations, power spectra of surface soil moisture showed a red noise-like $1/f^2$ scaling over a large scale range of time scales (1 h ≤ τ ≤ 1000 h), without any strong break in the scaling. The scaling exponents are rather homogeneous at the surface layer and exhibit some variability at deeper horizons where spectra tend to become steeper.

In a second step, multifractal analysis has been applied in order to identify the possible existence of scaling properties for non-quadratic moment orders. Multifractality has also been observed in the range of scales comprised between 1 h and 128 h. The moment scaling functions have been successfully fitted with the two-parameter functional form predicted by the Universal Multifractal Model. At the surface (5 cm depth) layer, the obtained parameters showed a slightly greater dispersion than that of spectral slopes, with $C_1 \approx 0.2$-0.3 and $\alpha \approx 1.3$-1.8 for surface data (5 cm depths). However, a greater dispersion has been found for data collected at deeper horizons (10-30 cm). On average, the depth affects the multifractality parameters more strongly than spectral slopes. At 30 cm depth, C_1 is closer to 0.4-0.5 while α often becomes smaller than 1. This shift and this variability could be related to the soil composition while surface parameters are likely to be more representative of the influence of the meteorological forcing.

Multiscale entropy has also been applied as a complementary scaling analysis tool devoted to the multiscale analysis of information content present in the series. This approach had been originally developed in Biology/medicine research literature and has a good potential for analyzing time series in other scientific fields. As noticed by Nogueira (2017), a systematic relationship exists between MSE scaling and spectral/first-order structure function scaling in the case of synthetic monofractal data and seems to hold for scaling geophysical observations.

MSE analysis has been performed over the twelve SMOSMANIA surface time series, showing the existence of scaling properties for the sample entropies estimated at various aggregation resolutions (30-650 hours). Due to the strong constraints on sample entropy estimation, the validity of MSE scaling at larger scales could not be investigated. This is a basic (methodological) limitation of the MSE approach that is compensated by other advantages: contrary to the usual structure function approach, MSE could be appropriate to analyze processes with negative Hurst scaling exponents (i.e. with $H < 0$ or $\beta < 1$) and has a rather direct interpretation in terms of information theory.

More generally, our numerical results also demonstrated that the MSE scaling properties are not limited to fBm-like *monofractals* investigated by previous authors (Gao et al., 2015; Nogueira, 2017) but should hold for synthetic and natural signals characterized by *multifractal* properties. Numerical tests were used to investigate the existence of a systematic relationship between the MSE scaling parameter H' and the three multifractal parameters H, C_1 and α. It has been observed that the relationship $H' = f(H, C_1, \alpha)$ is more complex than in the monofractal case (where $H' \approx H$) and that in some cases the intermittency parameter C_1 and the multifractality parameter α can affect significantly MSE scaling properties. In other cases (i.e. large H or low intermittency), the approximation $H' \approx H$ could be acceptable. Finally, more theoretical work remains to be done to understand the relationships between MSE scaling and fractal/multifractal scaling properties. This could open interesting perspectives for a better physical understanding of many geophysical processes that exhibit multifractal properties.

Acknowledgements

The International Soil Moisture Network (ISMN) and Météo France are gratefully thanked for providing the SMOSMANIA data through the ISMN website. Mathis Neuhauser from CESBIO is thanked for fruitful discussions.

References

Albergel, C., Rüdiger, C., Calvet, J.-C., Carrer, D., Fritz, N., Pellarin, T., 2010 (in French). Utilisation de mesures in situ d'humidité des sols pour l'évaluation de produits satellitaires micro-ondes dans le Sud-Ouest de la France. La Houille Blanche, 2, 120-126. doi : 10.1051/lhb 2010027.

Albergel, C., Zakharova, E., Calvet, J.-C. et al., 2011. A first assessment of the SMOS data in southwestern France using in situ and airborne soil moisture estimates: The CAROLS airborne campaign. Remote Sensing of Environment 115, 2718-2728. doi:10.1016/j.rse.2011.06.012.

Calvet, J.-C., Fritz, N., Froissard, F., Suquia, D., Petitpa, A., Piguet, B. 2007. In situ soil moisture observations for the CAL/VAL of SMOS: the SMOSMANIA network. Proceedings of the International Geoscience and Remote Sensing Symposium, IGARSS, Barcelona. doi:10.1109/IGARSS.2007.4423019.

Chambers, J.M., Mallows, C.L., Stuck, B.W., 1976. A method for simulating stable random variables. J. Amer. Statist. Assoc., 71, 340-344.

Corrsin, S., 1951. On the spectrum of isotropic temperature fluctuations in an isotropic turbulence. J. Appl. Phys. 22, 469–473.

Costa, M., Goldberger, A.L., Peng, C.K. , 2002. Multiscale entropy analysis of complex physiologic time series. Phys. Rev. Lett. 2002, 89. https://doi.org/10.1103/PhysRevLett.89.068102.

Costa, M., Peng, C.K., Goldberger, A.L. Haussdorff, J.M., 2003. Multiscale entropy analysis of human gait dynamics. Physica A 330, 53-60. doi:10.1016/j.physa.2003.08.022.

Costa, M., Goldberger A.L., Peng C.K., 2005. Multiscale entropy analysis of biological signals. Phys. Rev. E. 2005; 71: 021906. DOI: 10.1103/PhysRevE.71.021906

Courtiol, J., Perdikis, D., Petkoski, S., Muller, V., Huys, R., Sleimen-Malkoun, R., Jirsa, V.K., 2016. The multiscale entropy: Guidelines for use and interpretation in brain signal analysis. J. Neuro. Meth. 2016; 273: 175-190.

D'Errico, J., (2017). SLM – Shape Language Modelling Toolbox, accessible at: http://mathworks.com/matlabcentral/fileexchange/24443-slm-shape-language-modeling.

de Lima, M.I. P., Lovejoy, S., 2015. Macroweather precipitation variability up to global and centennial scales, Water Resour. Res., 51, 9490-9513. doi:10.1002/2015WR017455.

Dorigo, W. A., Wagner, W., Hohensinn, R., Hahn, S., Paulik, C., Xaver, A., Gruber, A., Drusch, M., Mecklenburg, S., van Oevelen, P., Robock, A., and Jackson, T., 2011. The International Soil Moisture Network: a data hosting facility for global in situ soil moisture measurements, Hydrol. Earth Syst. Sci., 15, 1675-1698, doi:10.5194/hess-15-1675-2011.

Entekhabi, D., Njoku, E.G., et al., 2010. The Soil Moisture Active Passive (SMAP) mission. Proceedings of the IEEE, 10.1109/JPROC.2010.2043918.

Farmer, J.D., Ott, E., Yorke, J.A., 1983. The dimension of chaotic attractors. Physica D: Nonlinear Phenomena, 7, issues 1-3, 153-180.

Fraedrich, K., Larnder, C., 1993. Scaling regimes of composite rainfall time series, Tellus, 45, 289-298.

Gagnon, J.S., Lovejoy, S., Schertzer, D., 2006. Multifractal Earth Topography. Nonlin. Processes Geophys. 13, 541-570.

Gao, J., Hu, J., Liu, F., Cao, Y., 2015. Multiscale entropy analysis of biological signals: a fundamental bi-scaling law. Front. Comput. Neurosci. 2015, 9: 64. https://doi.org/10.3389/fncom.2015.00064 .

Gires, A., Onof, C., Maksimovic, C., Schertzer, D., Tchiguirinskaia, I., Simoes, N., 2012. Quantifying the impact of small scale unmeasured rainfall variability on urban runoff through multifractal downscaling: A case study. Journal of Hydrology, 442-443, 117-128, http://dx.doi.org/10.1016/j.jhydrol.2012.04.005.

Hentschel, H.G.E. , Procaccia, I., 1983. The infinite number of generalized dimensions of fractals and strange attractors. Physica D, 8 (3), 435-444.

Katul, G., Porporato, A., Daly E., Oishi, C., Kim, H.-S., Stoy, P.C., Juang, J.Y., Siquira, M.B., 2007. On the spectrum of soil moisture from hourly to interannual scales. Water Resources Research, 43, W05428, doi:10.1029/2006WR005356.

Kerr, Y., Waldteufel, P., et al. 2010. The SMOS mission : new tool for monitoring key elements of the global water cycle. Proceedings of the IEEE, 98, 666–687. doi: 10.1109/JPROC.2010.2043032.

Kerr, Y., Al-Yaari, A., et al., 2016. Overview of SMOS performance in terms of global soil moisture monitoring after six years in operation. Remote Sensing of Environment 180, 40-63. http://dx.doi.org/10.1016/j.rse.2016.02.042.

Kim, G., Barros, B., 2002a. Space–time characterization of soil moisture from passive microwave remotely sensed imagery and ancillary data. Remote sensing of Environment 81, 393-403.

Kim, G., Barros, B., 2002b. Downscaling of remotely sensed soil moisture with a modified fractal interpolation method using contraction mapping and ancillary data. Remote sensing of Environment 83, 400-413.

Kolmogorov, A.N., 1941. Local structure of turbulence in an incompressible liquid for very large Reynolds numbers. Proc. Acad. Sci. URSS, Geochem. Sect. 30, 299–303.

Lavallée, D., 1991. Multifractal Techniques: Analysis and Simulation of Turbulent Fields. Ph. D. Thesis, McGill University, Montréal, Canada.

Lavallée, D., Lovejoy, S., Schertzer, D., Ladoy, P., 1993. Nonlinear variability of landscape topography: multifractal analysis and simulation. In: De Cola, L., Lam, N. (Eds.), Fractals and Geography. Prentice Hall, New Jersey, pp. 158–192.

Lovejoy, S., Schertzer, D., 2006. Multifractal, cloud radiances and rain. Journal of Hydrology, 322, 59-88, doi:10.1016/j.hydrol.2005.02.042.

Lovejoy, S., Schertzer, D., 2010. Towards a new synthesis for atmospheric dynamics: space-time cascades. Atmospheric Research, 96, 1-52. https://doi.org/10.1016/j.atmosres.2010.01.004

Lovejoy S., Schertzer D., 2012. Haar wavelets, fluctuations and structure functions: convenient choices for geophysics. Nonlin. Proc. Geophys., 19, 513-527.

Lovejoy, S., and Schertzer, D., 2013. The Weather and Climate: Emergent Laws and Multifractal Cascades, 496 pp., Cambridge University Press.

Lovejoy, S., Schertzer, D., Allaire, V., 2008. The remarkable wide range spatial scaling of TRMM precipitation. Atmos. Res. 90, 10–32.

Lovejoy, S., Tarquis, A.M., Gaonac'h, H., Schertzer, D.,2008. Single- and multiscale remote sensing techniques, multifractals, and MODIS-derived vegetation and soil moisture. Vadose Zone J. 7: 533–546.

Lovejoy, S., Schertzer, D., Varon, D., 2013. Do GCMs predict climate… or macroweather? Earth Syst. Dyn., 4, 439-454, doi:10.5194/esd-4-439-2013.

Loverro, A., 2004. Fractional calculus: history, definitions and applications for engineer. USA: Department of Aerospace and Mechanical Engineering, University of Notre Dame; 2004.p. 870–84.

Macor, J.L., 2007. Développement de techniques de prévision de pluie basées sur les propriétés multi-échelles des données radar et satellite. PhD Thesis (in French), Ecole Nationale des Ponts et Chaussées, Marne-la-Vallée, France.

Mandelbrot, B. B.: The Fractal Geometry of Nature, Freeman, NewYork, 1983.

Mascaro, G., Vivoni, E.R., 2010. Statistical and scaling properties of remotely-sensed soil moisture in two contrasting domains in the North American monsoon region. J. Arid Environ. 74: 572–578. doi:10.1016/j.jaridenv.2009.09.023.

Mascaro, G., Vivoni, E.R., 2012. Comparison of statistical and multifractal properties of soil moisture and brightness temperature from ESTAR and PSR during SGP99. IEEE Geosci. Remote Sens. Lett. 9: 373–377. doi: 10.1109/LGRS.2011.2169770.

Mascaro, G., Vivoni, E.R., Deidda, R., 2010. Downscaling soil moisture in the southern Great Plains through a calibrated multifractal model for land surface modeling applications. Water Resour. Res. 46. W08546, doi:10.1029/2009WR008855.

Mascaro, G., Vivoni, E.R., Deidda, R., 2011. Soil moisture downscaling across climate regions and its emergent properties. J. Geophys. Res. (Atm.) 116. D22114, doi:10.1029/2011JD016231.

Merlin, O., Walker, J.P., Chehbouni, A., Kerr, Y., 2008. Towards deterministic downscaling of SMOS soil moisture using MODIS derived soil evaporative efficiency. Remote Sensing of Environment, 112, 3935-3946. doi: 10.1016/j.rse.2008.06.012

Merlin, O., Rüdiger, C., Al Bitar, A., Richaume, P., Walker, J., Kerr, Y., 2012. Disaggregation of SMOS soil moisture in southeastern Australia. IEEE Transactions on Geoscience and Remote Sensing, 50, 1556-1571. doi: 10.1109/TGRS.2011.2175000

Neuhauser, M., Verrier, S., Mangiarotti, S., 2018. Propriétés statistiques multi-échelles de produits satellitaires SMOS d'humidité du sol désagrégés à la résolution kilométrique (in French). Proc. of Rencontres du Non-Linéaire 2018, Paris, France.

Nogueira, M., 2017. Exploring the link between multiscale entropy and fractal scaling behavior in near-surface wind. PLoS ONE 12(3):e0173994. https://doi.org/10.1371/journal.pone.0173994.

Obukhov, A.M., 1949. Structure of the temperature field in a turbulent flow. Izv. Akad. Nauk S.S.S.R, Ser Geograf. Geofiz. 13, 58–69.

Olsson, J., 1995. Limits and characteristics of the multifractal behaviour of a high-resolution rainfall time series. Nonlin. Proc. Geophys., 2(1), 23-29.

Pandey, G., Lovejoy, S., Schertzer, D., 1998. Multifractal analysis of daily river flows including extremes for basins of five to two million square kilometers, onde day to 75 years. Journal of Hydrology 208, 62-81.

Pelletier, J.D., Malamud, B.D., Blodgett, T., Turcotte, D.L., 1997. Scale-invariance of soil moisture variability and its implicationsfor the frequency-size distribution of landslides. Engineering Geology 48, 255-268.

Richman, J.S., Moorman, J.R.,2000. Physiological time-series analysis using approximate entropy and sample entropy. Am. J. Physiol. Heart. Circ. Physiol. 2000; 278: H2039-H2049

Schertzer, D., Lovejoy, S., 1987. Physical modelling and analysis of rain and clouds by anisotropic scaling multiplicative processes. J. Geophys. Res. 92 (D8), 9693–9714.

Schertzer, D., Lovejoy, S., 1991. Nonlinear geodynamical variability: multiple singularities, universality and observables. In: Nonlinear Variability in Geophysics, D. Schertzer and S. Lovejoy (eds.), Kluwer, Netherlands, 1991, p. 41-82.

Schertzer, D., Lovejoy, S., 1997. Universal multifractals do exist! J. Appl. Meteorol.,36, 1296–1303.

Schertzer, D., Lovejoy, S., Hubert, P., 2002. An introduction to stochastic multifractal fields. In: Ern, A., Weiping, L. (Eds.), Mathematical Problems in Environmental Science and Engineering. Series in Contemporary Applied Mathematics, vol. 4. Higher Education Press, Beijing, pp. 106–179.

She Z. S., Levêque, E. (1994), Universal scaling laws in fully developed turbulence, Phys. Rev. Lett., 72, 336–339.

Tessier, Y., Lovejoy, S., Schertzer, D., 1993. Universal multifractals in rain and clouds: theory and observations. J. Appl. Meteorol. 32, 223–250

Vereecken, H., Huisman, J.A., Pachepsky, Y., Montzka, C., van der Kruk, J., Bogena, H., Weihermüller, L., Herbst, M., Martinez, G., Vanderborght, J., 2014. On the spatio-temporal dynamics of soil moisture at the field scale. Journal of Hydrology 516, 76-96. http://dx.doi.org/10.1016/j.jhydrol.2013.11.061

Verrier, S., Mallet, C., and Barthès, L. (2011), Multiscaling properties of rain in the time domain, taking into account rain support biases. Journal of Geophysical Research, 116, D20119, http://dx.doi.org/10.1029/2011JD015719.

Verrier, S., Crépon, M., Thiria, S. (2014), Scaling and stochastic cascade properties of NEMO oceanic simulations and their potential value for GCM evaluation and downscaling, J. Geophys. Res. Oceans, 119, 6444–6460, doi:10.1002/2014JC009811.

Zhang, Y.C., 1991. Complexity and 1/f noise. A phase space approach. J. Phys. I. 1991, 1(7): 971-977.

Tables

Station	GPS coordinates (Lat/Lon)		Altitude (m)	Sensor
Condom	43.97440	0.33610	174	ThetaProbe-ML2X
Créon d'Armagnac	43.99360	-0.04690	149	ThetaProbe-ML2X
Lahas	43.54720	0.88780	249	ThetaProbe-ML2X
Lézignan Corbieres*	43.17330	2.72830	60	ThetaProbe-ML2X
Montaut	43.19220	1.64360	295	ThetaProbe-ML2X
Mouthoumet	42.96000	2.53000	538	ThetaProbe-ML2X
Narbonne	43.15000	2.95670	112	ThetaProbe-ML2X
Peyrusse Grande	43.66640	0.22170	245	ThetaProbe-ML2X
Sabres*	44.14750	-0.84560	81	ThetaProbe-ML2X
St Félix de Lauragais*	43.44170	1.88000	337	ThetaProbe-ML2X
Savenès	43.82500	1.17670	158	ThetaProbe-ML2X
Urgons	43.63970	-0.43500	145	ThetaProbe-ML2X

Table 1a : Identification of the 12 SMOSMANIA stations located in the region of interest. Names marked with a star correspond to stations that are not used in the rest of the study.

Station	Soil texture
Condom	Clay
Créon d'Armagnac	Sand
Lahas	Clay
Lézignan Corbieres	Silt loam
Montaut	Silt loam
Mouthoumet	Silt loam
Narbonne	Silt loam
Peyrusse Grande	Clay
Sabres	Sand
St Félix de Lauragais	Clay
Savenès	Silt loam
Urgons	Silt loam

Table 1b : Soil texture classification (in terms of USDA texture classification), based on ISMN/SMOSMANIA metadata information.

Station	**β**	**Δβ**	**R^2**
Condom	1.99	0.037	0.988
Créon d'Armagnac	2.01	0.037	0.988
Lahas	1.96	0.039	0.987
Montaut	1.97	0.034	0.990
Mouthoumet	2.02	0.036	0.989
Narbonne	1.91	0.034	0.989
Peyrusse Grande	1.93	0.031	0.991
Savenès	1.92	0.030	0.992
Urgons	1.99	0.036	0.989

Table 2: Estimates of spectral scaling exponents β for the time series collected at 5 cm depth. Δβ is half of the length of the 95% confidence interval on β while the last column presents the coefficient of determination.

Station	C_1	α	Validity conditions
Condom	0.22	1.82	$q \leq 2.5$; scales 1-128 h
Créon d'Armagnac	0.26	1.42	«
Lahas	0.27	1.82	«
Montaut	0.31	1.60	«
Mouthoumet	0.22	1.76	«
Narbonne	0.31	1.61	«
Peyrusse Grande	0.28	1.51	«
Savenès	0.27	1.68	«
Urgons	0.29	1.37	«

Table 3: Universal multifractal parameter estimates for the nine SMOSMANIA time series collected at 5 cm depth.

Station	*H'*	*ΔH'*	R^2
Condom	0.31	0.02	0.96
Créon d'Armagnac	0.45	0.02	0.99
Lahas	0.35	0.02	0.98
Montaut	0.38	0.02	0.98
Mouthoumet	0.35	0.04	0.90
Narbonne	0.66	0.02	0.99
Peyrusse Grande	0.36	0.02	0.96
Savenès	0.61	0.01	0.99
Urgons	0.36	0.01	0.98

Table 4: MSE scaling parameter estimates over the time scale range 30 h – 650 h for the nine series collected at 5 cm depth.

Station	*H*	*ΔH*	R^2
Condom	0.42	< 0.01	0.98
Créon d'Armagnac	0.37	"	0.97
Lahas	0.41	"	0.98
Montaut	0.41	"	0.99
Mouthoumet	0.39	"	0.96
Narbonne	0.38	"	0.93
Peyrusse Grande	0.39	"	0.98
Savenès	0.47	"	0.99
Urgons	0.42	"	0.99

Table 5: Structure function scaling parameter estimates over the time scale range 30 h – 650 h for the nine stations (surface moisture).

Figures captions

Figure 1: Power spectral densities $E(f)$ of the nine selected SMOSMANIA surface (5 cm depth) soil moisture series in logarithmic coordinates. In order to facilitate the understanding in terms of time scales, the horizontal axis exhibits values of $1/f$ (time scale equivalent to a Fourier frequency). The horizontal axis is presented so that high frequencies (i.e., small time scales) appear on the right of the figure. *The different curves have regularly been translated upwards in order to improve readability*.

Figure 2a: Power spectra of soil moisture at Peyrusse Grande, one spectrum per depth.

Figure 2b: Power spectra of soil moisture at Montaut, one spectrum per depth.

Figure 3: Estimates of spectral slope β for all stations and depths. Each line is associated to a depth. On the abscissa axis, the three letters identify the stations. Stations are sorted from west to east.

Figure 4: Flux moments estimated for the Peyrusse Grande time series of surface soil moisture. Logarithmic scales are used. Moment orders q vary between 0 and 2.5.

Figure 5: Flux moments estimates for the eight other surface soil moisture series. Again, moments orders comprised between 0 and 2.5 are represented.

Figure 6: Moment scaling function $K(q)$ of Peyrusse Grande surface soil moisture series.

Figure 7: Moments scaling functions $K(q)$ estimated for the eight other SMOSMANIA surface soil moisture series.

Figure 8: (**Upper figures and bottom left**) Moments estimations based on Peyrusse Grande data at depths 10, 20 and 30 cm. (**Bottom right**) Moments scaling functions estimated from depths 5, 10, 20 and 30cm.

Figure 9a: estimates of the index of multifractality α for the different stations and depths. Each line is associated to a depth. On the abscissa axis, the three letters identify the stations. Stations are sorted from west to east.

Figure 9b: estimates of the inhomogeneity parameter C_1 for the different stations and depths. Each line is associated to a depth. On the abscissa axis, the three letters identify the stations. Stations are sorted from west to east.

Figure 10: MSE analysis for the nine surface soil moisture series. For each series, the Sample Entropy (SampEn) is estimated for different time resolutions obtained by time aggregation. *Plots are shifted vertically from one station to one another to improve readability*.

Figure 11: MSE scaling parameter estimates over the time scale range 30 h – 650 h for the nine stations and the four depths considered.

Figure 12: First-order structure functions obtained for the nine SMOSMANIA series. *Plots are shifted vertically in order to improve readability.* The different curves are sorted in the same order as in Figure 10 (from Condom at the bottom to Urgons at the top).

Figure 13: Comparison of scaling exponents *H* and *H*' provided by SF and MSE methods.

Figure 14: MSE analysis for two synthetic multifractal time series generated with $H = 0$ (blue curve) and $H = 0.4$, for the same random realization. C_1 and α are respectively fixed to 0.05 and 2. Note that contrary to Figs. 1, 2 and 12, no vertical shift is applied here between both curves.

Figure 15: MSE analysis for two synthetic multifractal time series generated with $C_1 = 0.05$ (blue curve) and $C_1 = 0.35$, for the same random realization. *H* and α are respectively fixed to 0 and 2.

Figure 16: Estimated scaling parameter *H*' from the MSE analysis averaged on 20 random realizations. α is equal to 2 in these simulations. Each curve represents the evolution of H' as a function of *H* for a fixed C_1. The values of C_1 are the following: 0.05 (continuous blue curve), 0.15 (dashed blue curve), 0.25 (continuous red curve), 0.35 (dashed red curve), 0.45 (continuous green curve), 0.55 (dashed green curve). *H* is sampled from 0 to 0.7 with 0.1 spacing.

Figure 17: Estimated scaling parameter *H*' from the MSE analysis averaged on 20 random realizations. C_1 is equal to 0.25 in these simulations. Each curve represents the evolution of *H*' as a function of *H* for a fixed α. The values of α are the following: 1.5 (continuous blue curve), 1.6 (dashed blue curve), 1.7 (continuous red curve), 1.8 (dashed red curve), 1.9 (continuous green curve), 2 (dashed green curve). *H* is sampled from 0 to 0.7 with 0.1 spacing.

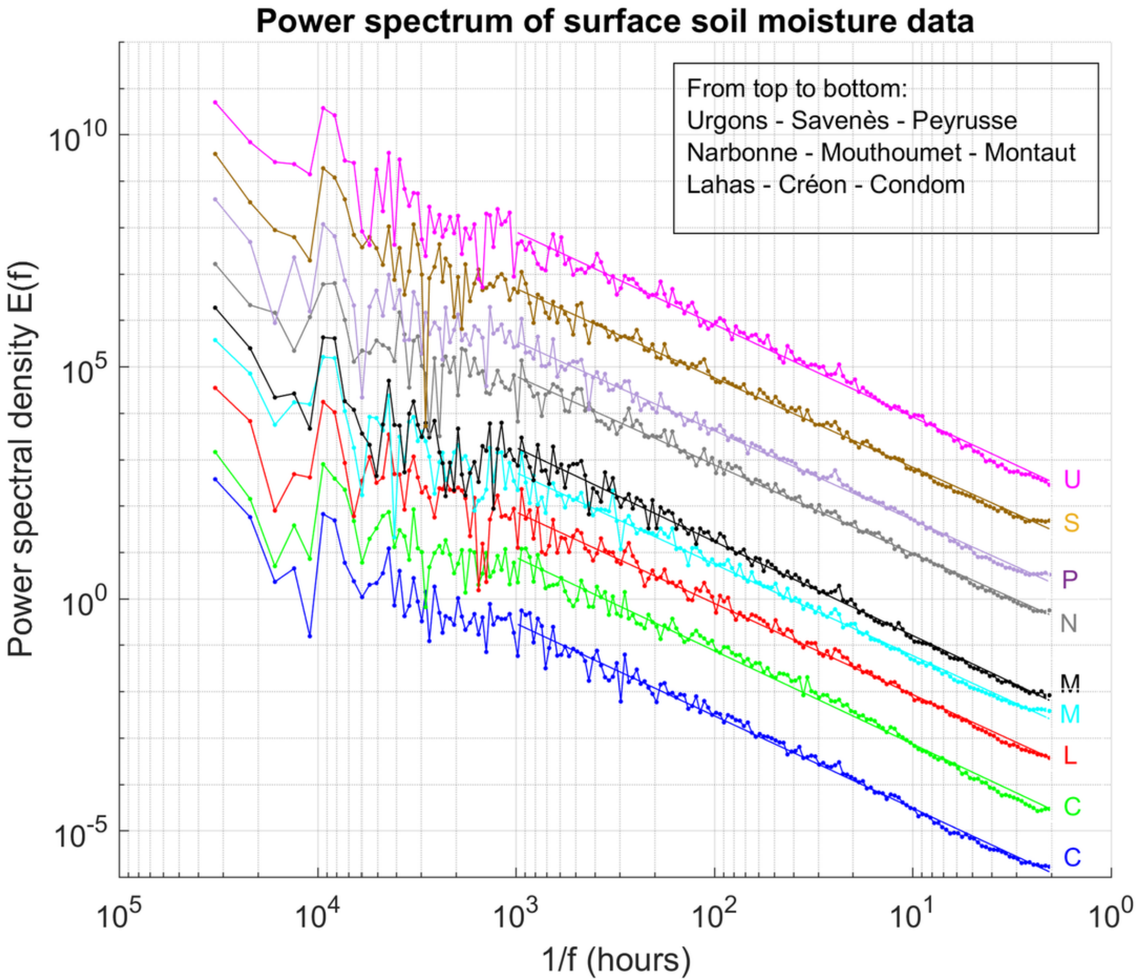

Power spectrum of surface soil moisture data
From top to bottom:
Urgons - Savenès - Peyrusse
Narbonne - Mouthoumet - Montaut
Lahas - Créon - Condom
Power spectral density E(f)
1/f (hours)
U
S
P
N
M
M
L
C
C

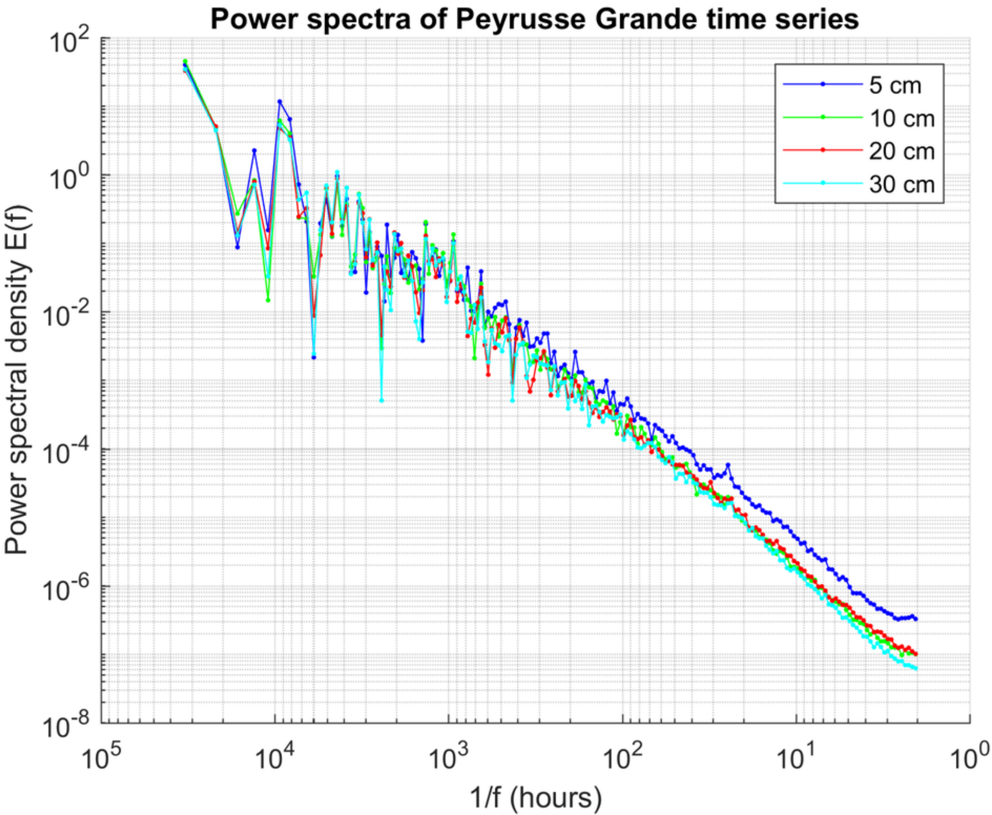

Power spectra of Peyrusse Grande time series
Power spectral density E(f)
1/f (hours)
5 cm
10 cm
20 cm
30 cm
10^2
10^0
10^{-2}
10^{-4}
10^{-6}
10^{-8}
10^5
10^4
10^3
10^2
10^1
10^0

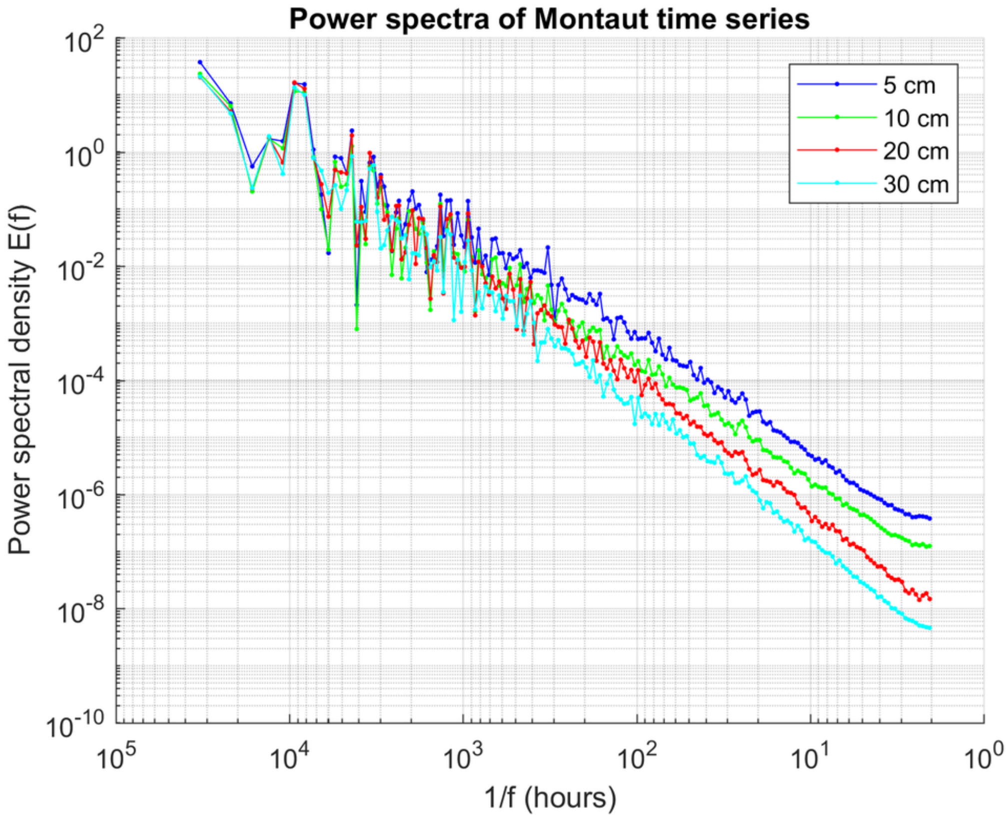
Power spectra of Montaut time series
Power spectral density E(f)
1/f (hours)
5 cm
10 cm
20 cm
30 cm
10^{2}
10^{0}
10^{-2}
10^{-4}
10^{-6}
10^{-8}
10^{-10}
10^{5}
10^{4}
10^{3}
10^{2}
10^{1}
10^{0}

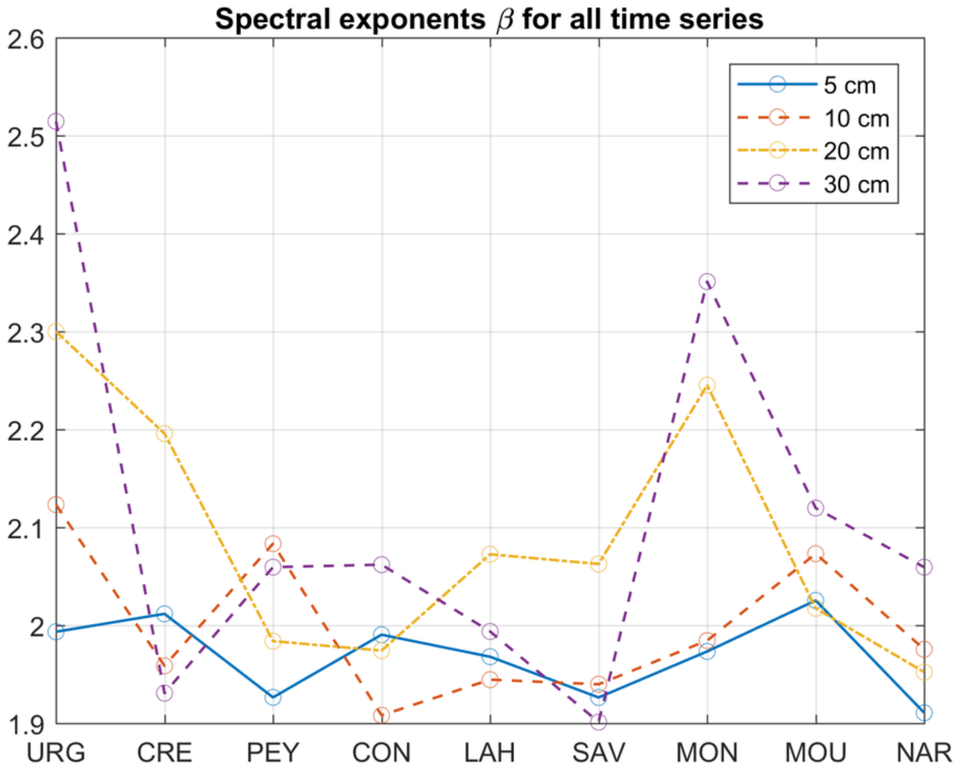
Spectral exponents β for all time series
2.6
2.5
2.4
2.3
2.2
2.1
2
1.9
URG
CRE
PEY
CON
LAH
SAV
MON
MOU
NAR
5 cm
10 cm
20 cm
30 cm

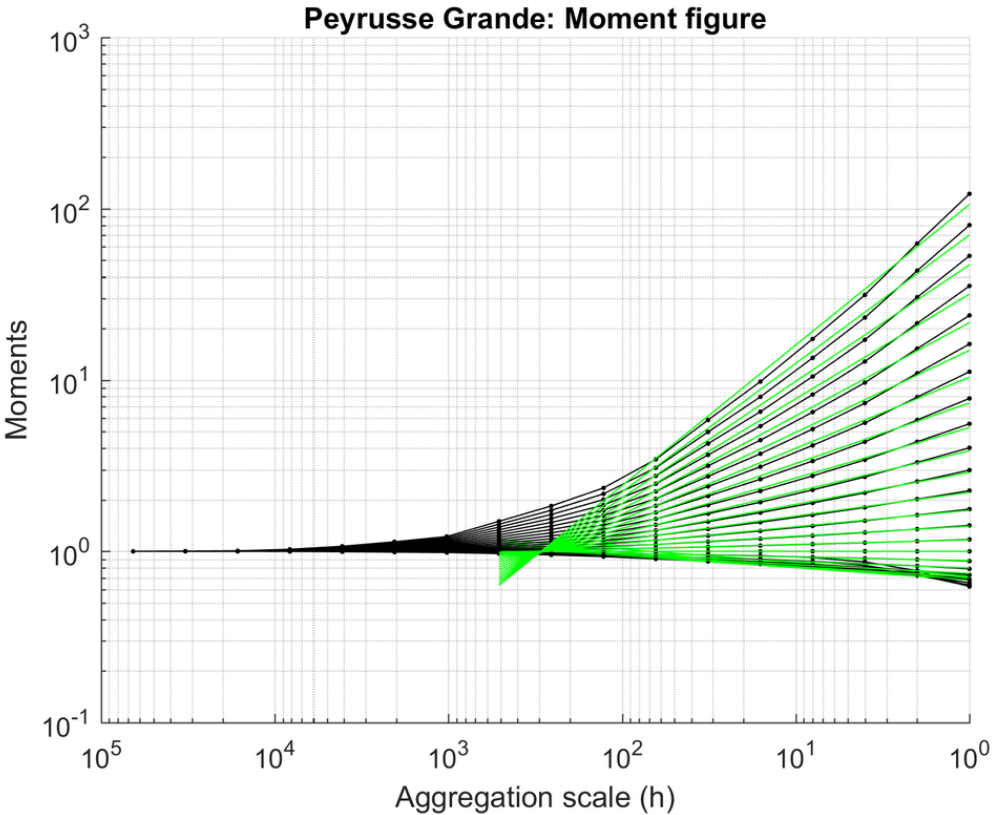
Peyrusse Grande: Moment figure
Moments
Aggregation scale (h)
10^3
10^2
10^1
10^0
10^{-1}
10^5
10^4
10^3
10^2
10^1
10^0

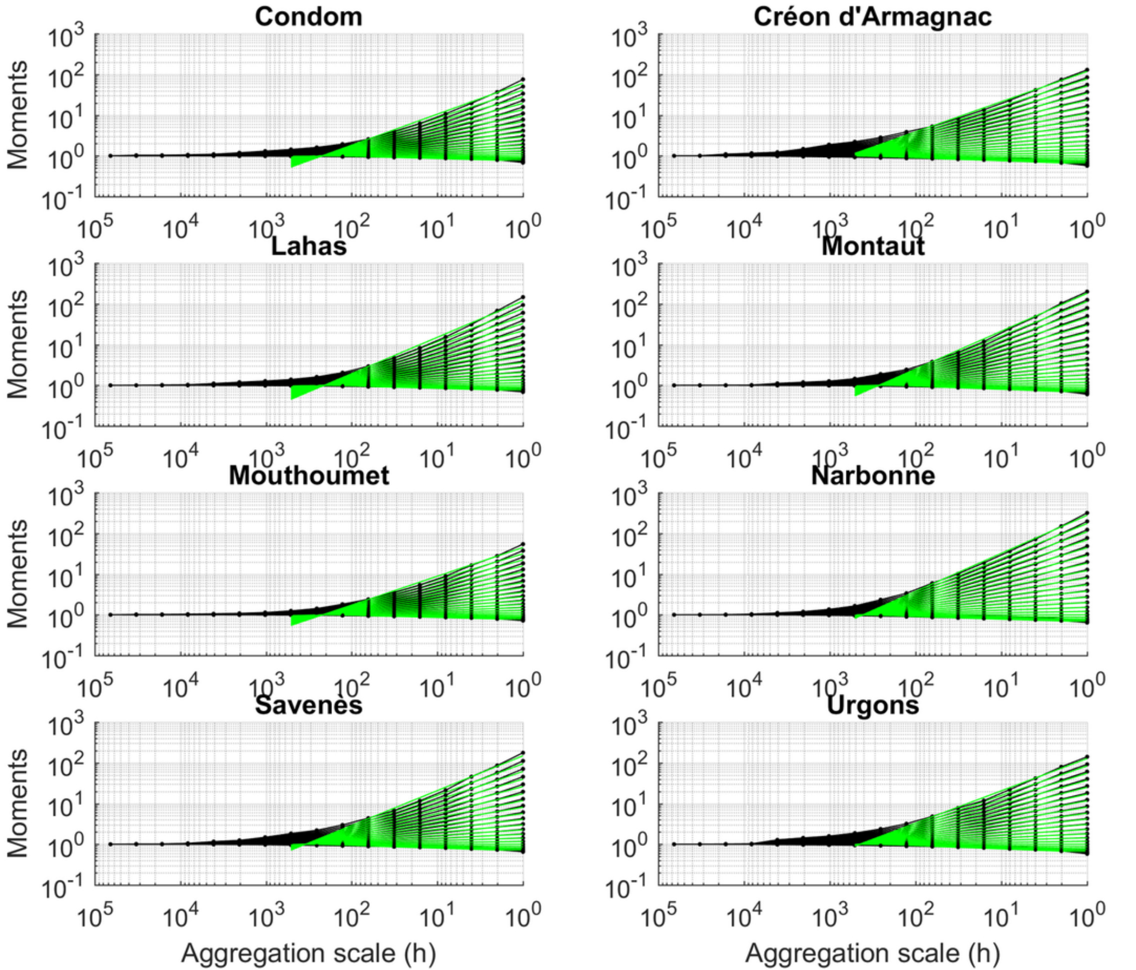
Condom
Créon d'Armagnac
Lahas
Montaut
Mouthoumet
Narbonne
Savenès
Urgons
Moments
Aggregation scale (h)

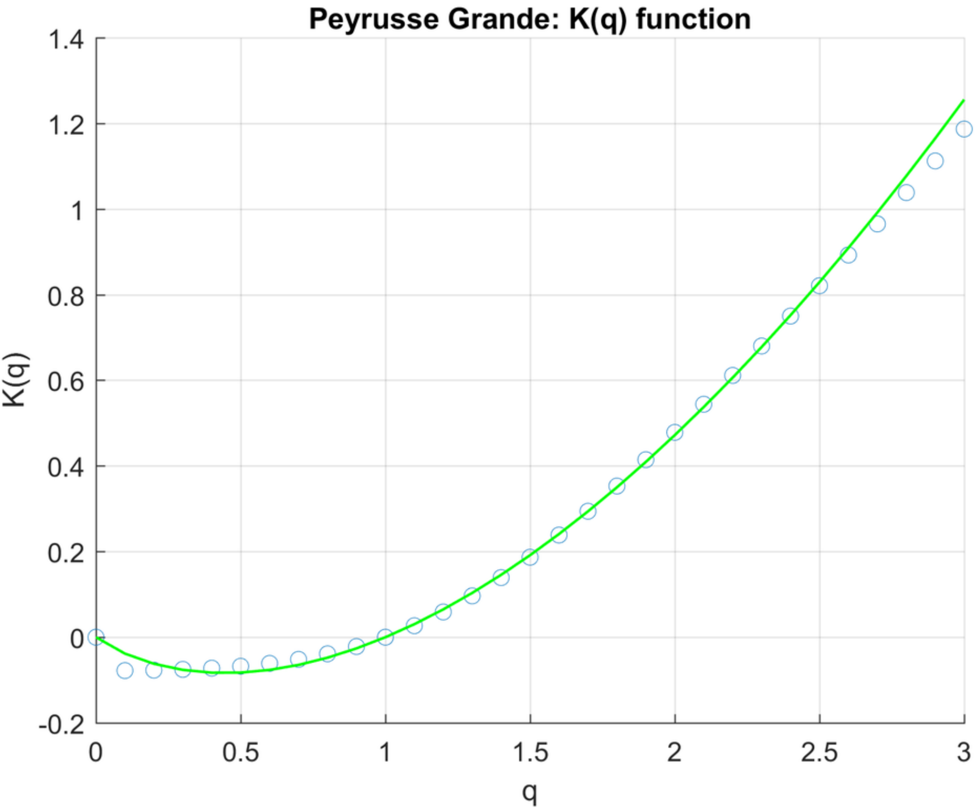
Peyrusse Grande: K(q) function
K(q)
q
1.4
1.2
1
0.8
0.6
0.4
0.2
0
-0.2
0
0.5
1
1.5
2
2.5
3

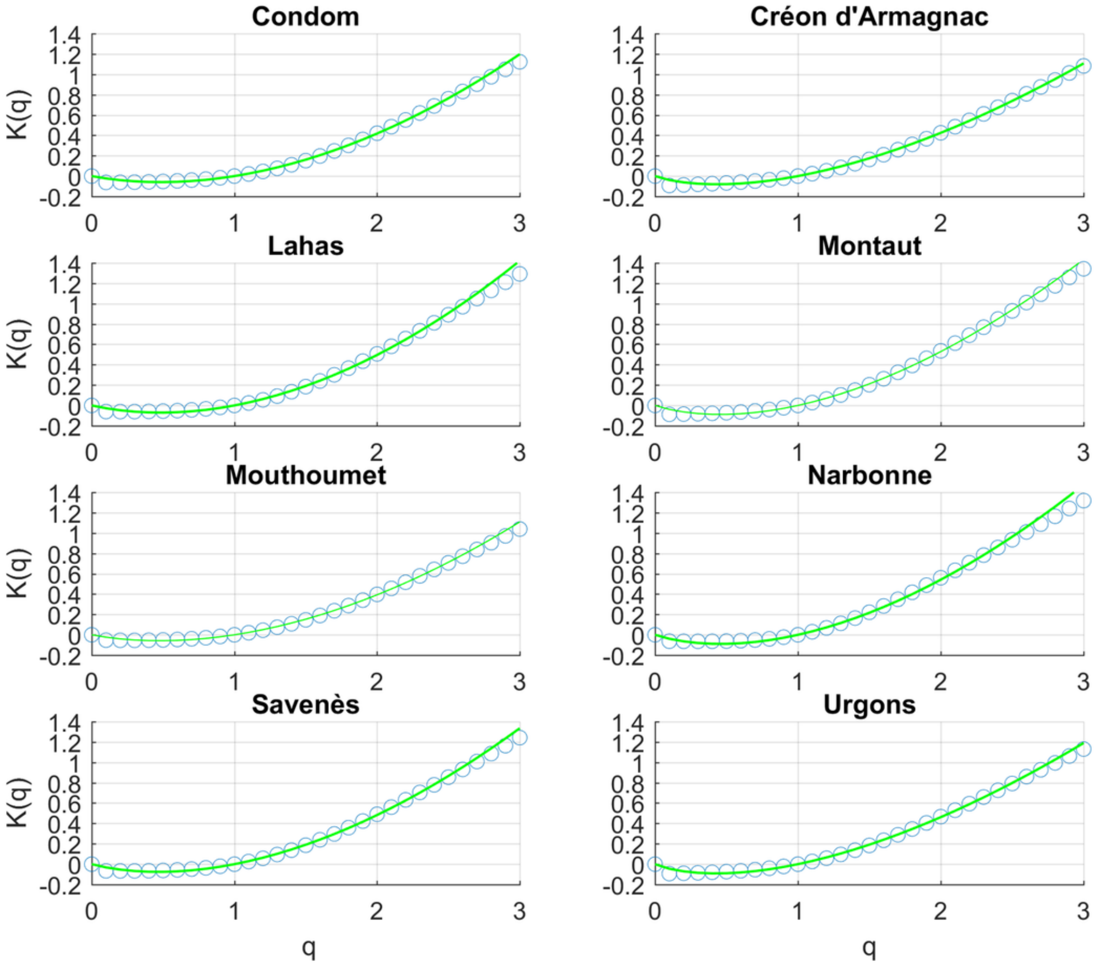
Condom
Créon d'Armagnac
Lahas
Montaut
Mouthoumet
Narbonne
Savenès
Urgons
K(q)
q
1.4
1.2
1
0.8
0.6
0.4
0.2
0
-0.2
0
1
2
3

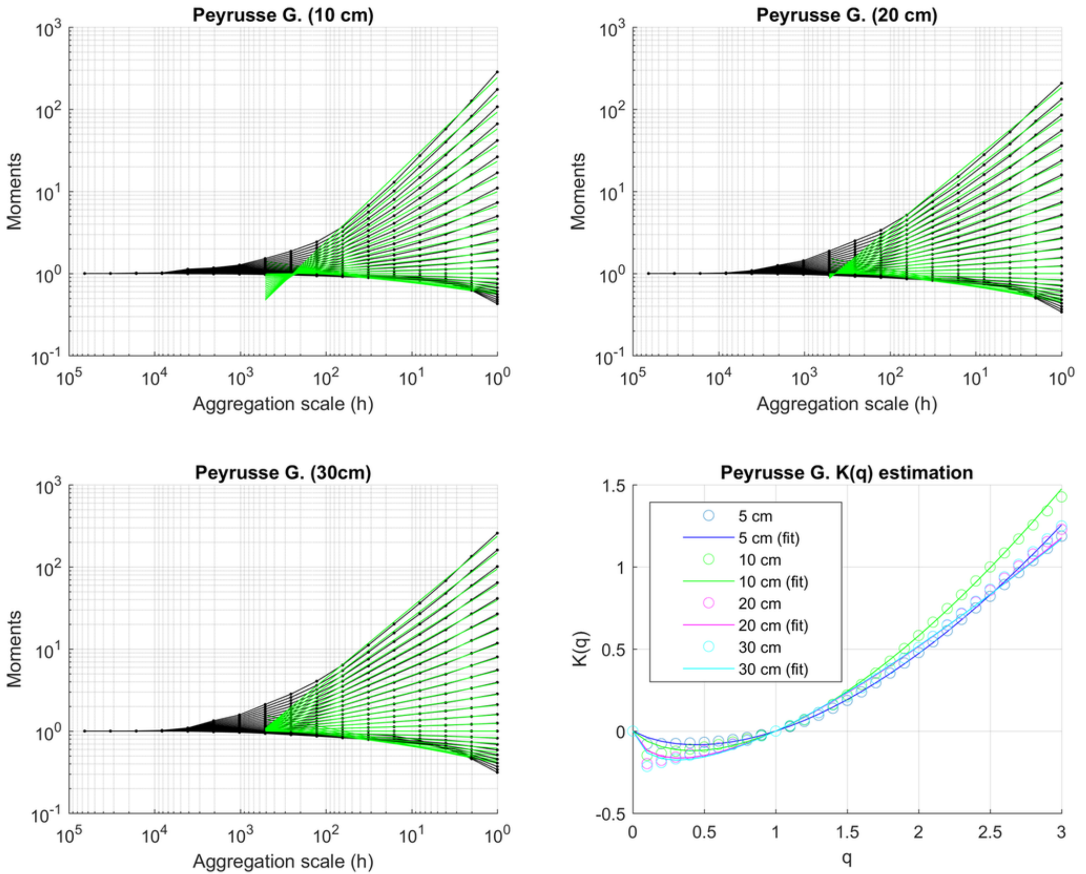

Peyrusse G. (10 cm)
Peyrusse G. (20 cm)
Peyrusse G. (30cm)
Moments
Aggregation scale (h)
Peyrusse G. K(q) estimation
K(q)
q
5 cm
5 cm (fit)
10 cm
10 cm (fit)
20 cm
20 cm (fit)
30 cm
30 cm (fit)

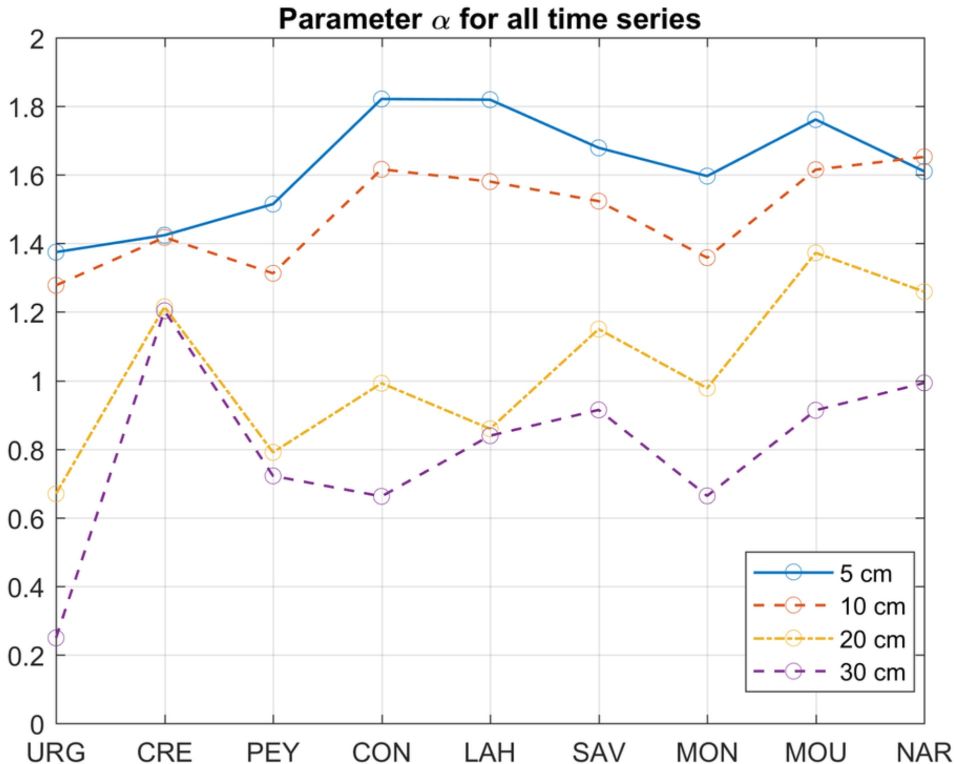

Parameter α for all time series
2
1.8
1.6
1.4
1.2
1
0.8
0.6
0.4
0.2
0
URG
CRE
PEY
CON
LAH
SAV
MON
MOU
NAR
5 cm
10 cm
20 cm
30 cm

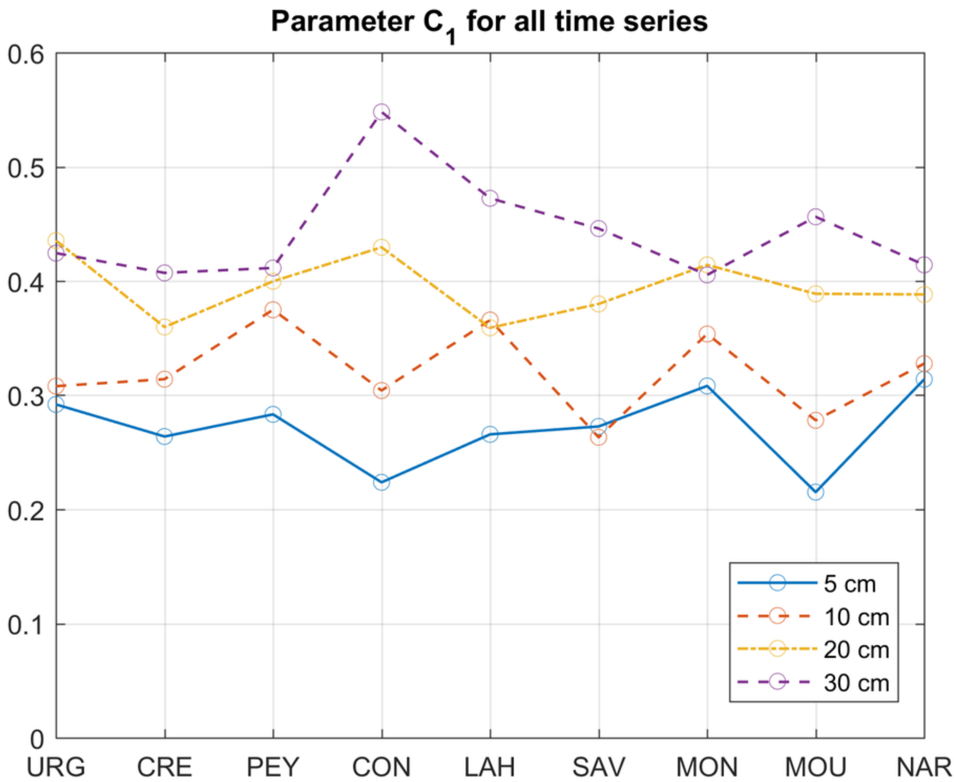
Parameter C_1 for all time series
0.6
0.5
0.4
0.3
0.2
0.1
0
URG
CRE
PEY
CON
LAH
SAV
MON
MOU
NAR
5 cm
10 cm
20 cm
30 cm

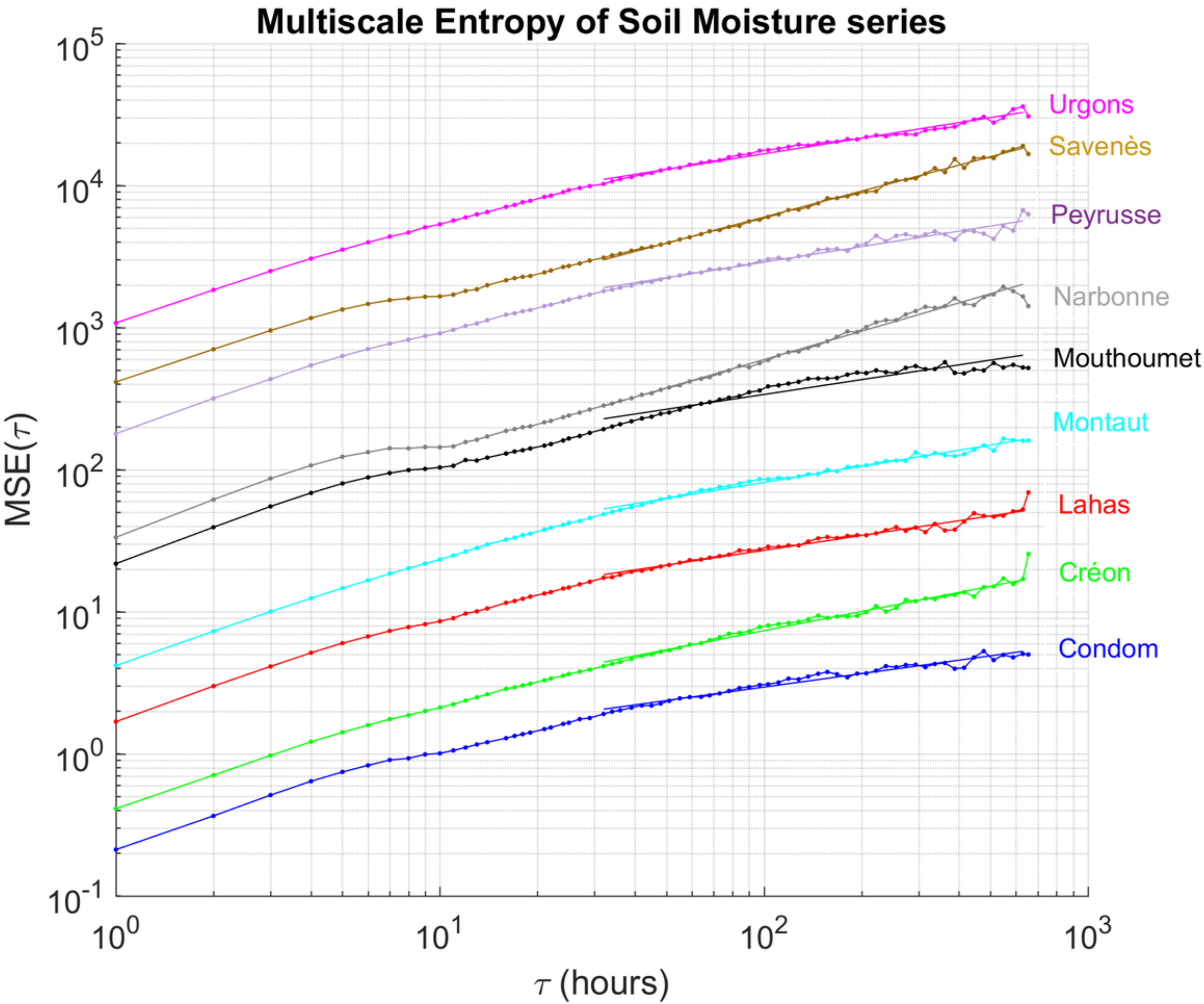

Multiscale Entropy of Soil Moisture series
MSE(τ)
τ (hours)
10^{-1}
10^{0}
10^{1}
10^{2}
10^{3}
10^{4}
10^{5}
Urgons
Savenès
Peyrusse
Narbonne
Mouthoumet
Montaut
Lahas
Créon
Condom

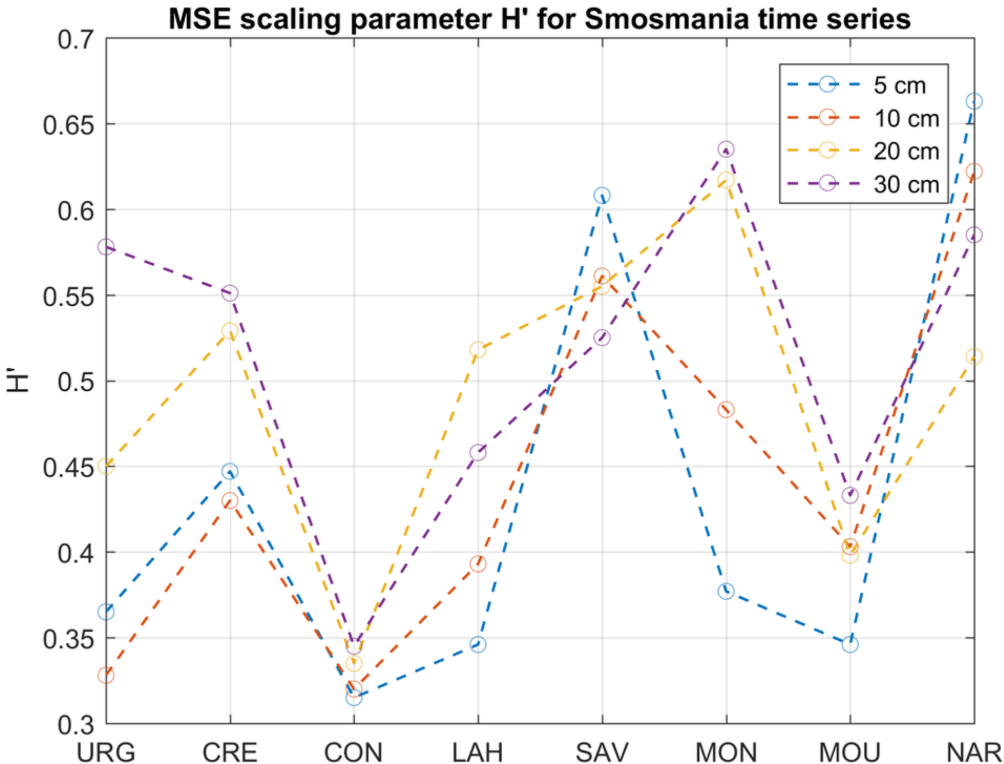
MSE scaling parameter H' for Smosmania time series
H'
0.7
0.65
0.6
0.55
0.5
0.45
0.4
0.35
0.3
URG
CRE
CON
LAH
SAV
MON
MOU
NAR
5 cm
10 cm
20 cm
30 cm

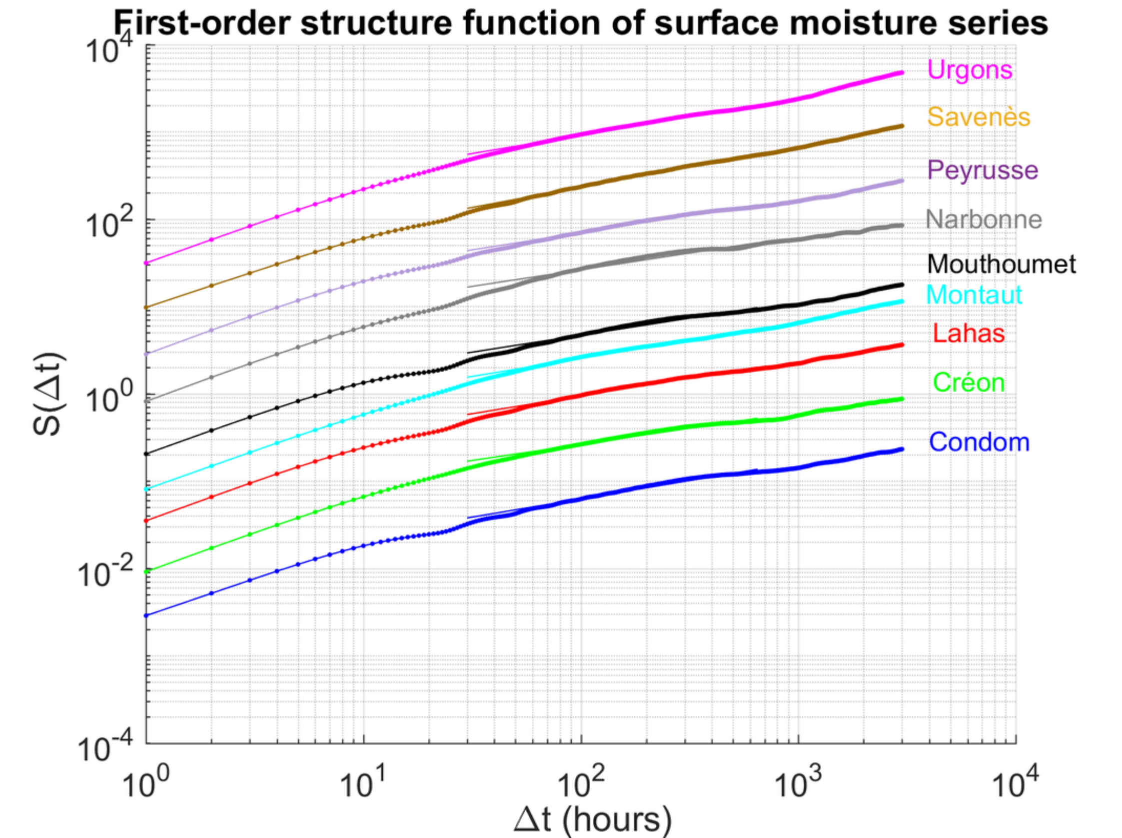

First-order structure function of surface moisture series
Urgons
Savenès
Peyrusse
Narbonne
Mouthoumet
Montaut
Lahas
Créon
Condom
S(Δt)
Δt (hours)

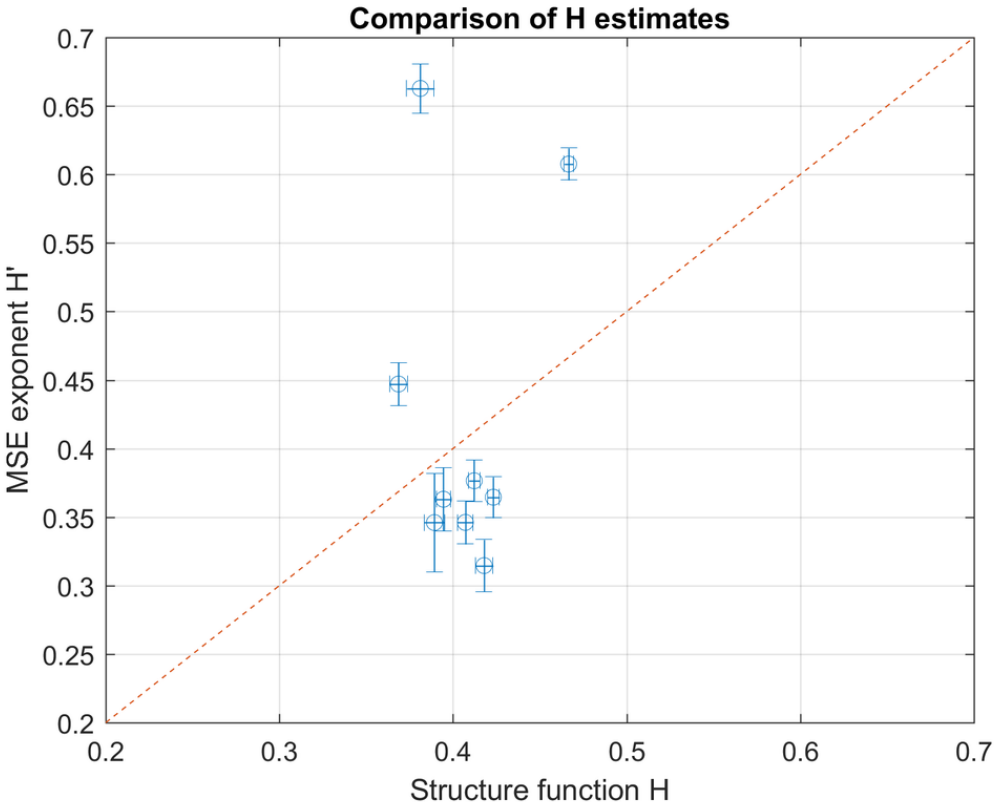
Comparison of H estimates
MSE exponent H'
Structure function H
0.2
0.25
0.3
0.35
0.4
0.45
0.5
0.55
0.6
0.65
0.7
0.2
0.3
0.4
0.5
0.6
0.7

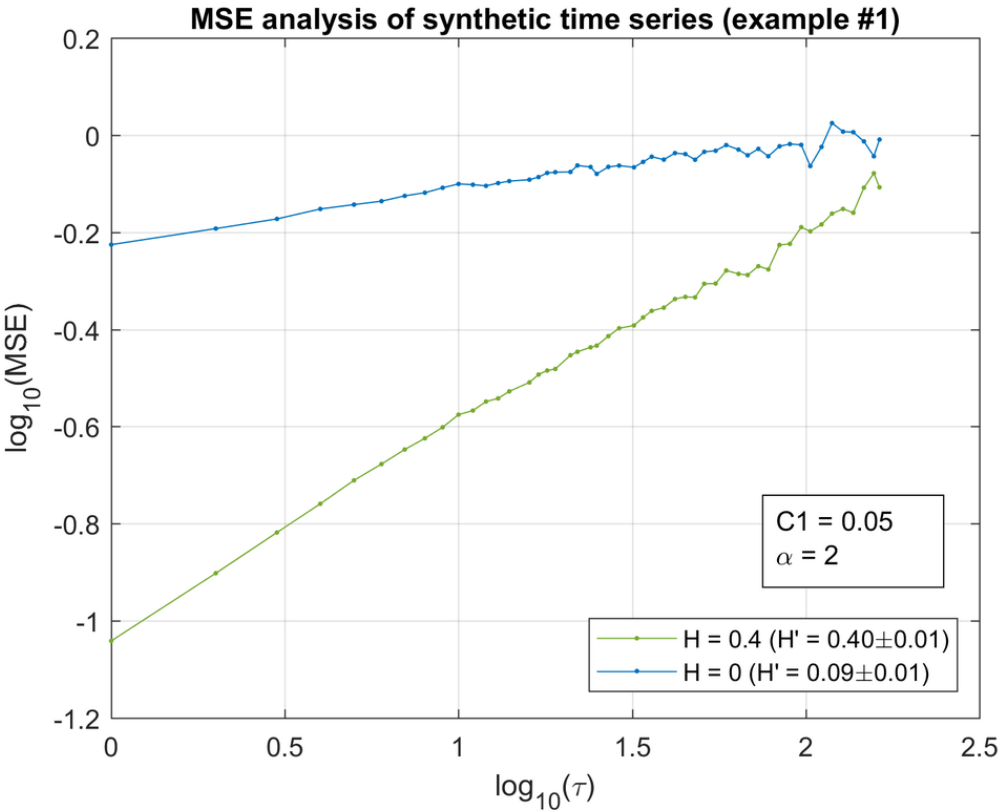
MSE analysis of synthetic time series (example #1)
0.2
0
-0.2
-0.4
-0.6
-0.8
-1
-1.2
log10(MSE)
0
0.5
1
1.5
2
2.5
log10(τ)
C1 = 0.05
α = 2
H = 0.4 (H' = 0.40±0.01)
H = 0 (H' = 0.09±0.01)

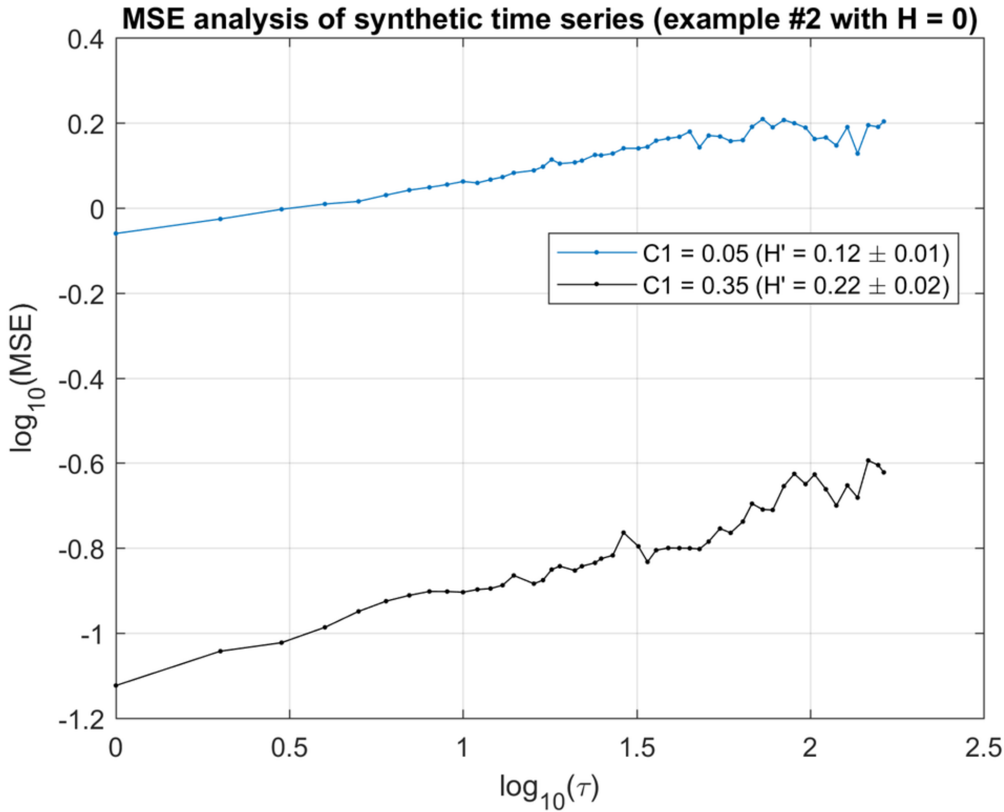
MSE analysis of synthetic time series (example #2 with H = 0)
0.4
0.2
0
-0.2
-0.4
-0.6
-0.8
-1
-1.2
0
0.5
1
1.5
2
2.5
log10(MSE)
log10(τ)
C1 = 0.05 (H' = 0.12 ± 0.01)
C1 = 0.35 (H' = 0.22 ± 0.02)

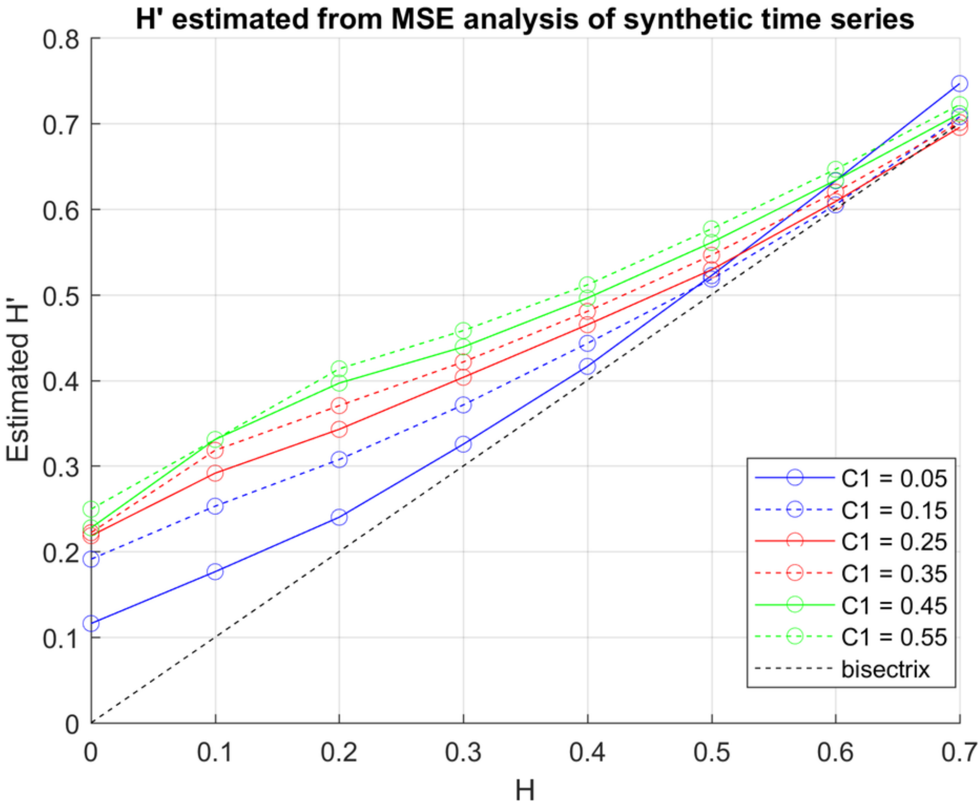

H' estimated from MSE analysis of synthetic time series
Estimated H'
H
0
0.1
0.2
0.3
0.4
0.5
0.6
0.7
0.8
C1 = 0.05
C1 = 0.15
C1 = 0.25
C1 = 0.35
C1 = 0.45
C1 = 0.55
bisectrix

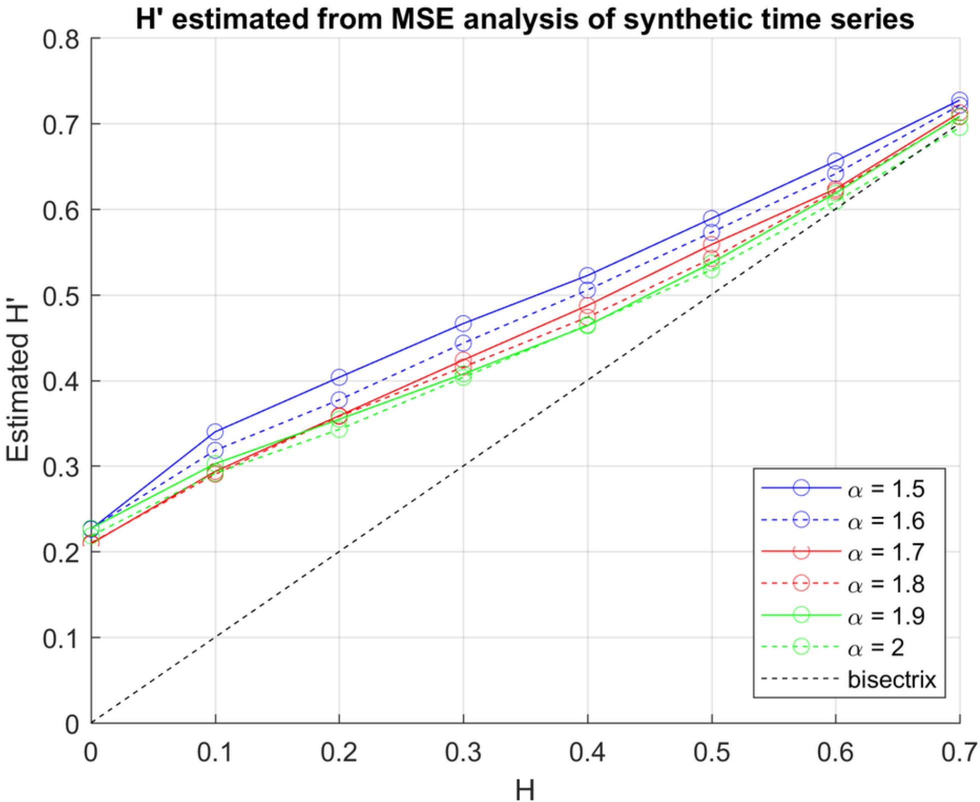
H' estimated from MSE analysis of synthetic time series
Estimated H'
H
0
0.1
0.2
0.3
0.4
0.5
0.6
0.7
0.8
α = 1.5
α = 1.6
α = 1.7
α = 1.8
α = 1.9
α = 2
bisectrix